universität wien

MASTERARBEIT / MASTER'S THESIS

Titel der Masterarbeit / Title of the Master's Thesis

„An update on arsenic and thallium mineralogy from the waste dumps of Crven Dol locality, Allchar deposit, North Macedonia“

verfasst von / submitted by

Annette Kathrin Steinfeld, BSc

angestrebter akademischer Grad / in partial fulfilment of the requirements for the degree of

Master of Science (MSc)

Wien, 2022 / Vienna 2022

Studienkennzahl lt. Studienblatt / degree programme code as it appears on the student record sheet:	UA 066 815
Studienrichtung lt. Studienblatt / degree programme as it appears on the student record sheet:	Masterstudium Erdwissenschaften UG2002
Betreut von / Supervisor:	Mag. Dr. Tamara Đorđević, Privatdoz.

Schau Mama, I did it!!

„O Bär“, sagte der Tiger, „ist das Leben nicht unheimlich schön, sag!“
„Ja“, sagte der kleine Bär, „ganz unheimlich und schön.“

aus Janosch. Post für den Tiger.

Acknowledgments

Die Lage der Welt, und meine im speziellen, hat sich in den letzten zwei Jahren massiv geändert und war geprägt von so großen, gewaltigen Dingen, die sich alle parallel ereigneten. Inmitten dessen habe ich begonnen meine Masterarbeit zu schreiben und wusste die meiste Zeit nicht wo Oben oder Unten ist.

Ohne die Unterstützung meiner Betreuerin Mag. Dr. Tamara Đorđević hätte ich diese Arbeit nicht fertig stellen können. Danke Tamara! Danke dass du mich jedes Mal wieder motivieren konntest, mir Freiheiten gegeben hast, wenn ich Sie gebaucht habe und mir strukturierte Aufgaben erteilt hast, wenn ich nicht weiter wusste. Ich habe viel von dir gelernt, nicht nur wissenschaftlich, sondern auch zwischenmenschliche Life-Hacks, danke dafür! *Draga Tamara, ovo su iskrene reči; bez tebe ne bih ovo sve uspela. Hvala od srca na svemu.*

Zur wissenschaftlichen Unterstützung dieser Arbeit muss ich im Weiteren, speziell Mag. Peter Nagl und Privat.-Doz. Dr. Uwe Kolitsch nennen. Uwe hat mir ermöglicht im Covid-Wahn, meine Messungen am Rasterelektronenmikroskop, am Naturhistorischen Museum in Wien, durchzuführen. Vielen Dank für die vielen lehrreichen Stunden am Mikroskop, die Erklärung zur Methodik und überhaupt für den wissenschaftlichen Input für diese Arbeit.

Peter hat mir nicht nur die grundlegenden Dinge der Probenvorbereitung und der RFA-Analyse beigebracht, er stand mir auch die komplette Zeit meiner Masterarbeit stets mit Rat und Tat zur Seite. Vielen Dank dir!

Zu guter Letzt möchte ich mich auch noch bei Prof. Dr. Christian Lengauer bedanken, für die zuvorkommende Unterstützung bei der Präparatsvorbereitung und der Erklärung der Methodik der Röntgen-Pulverdiffraktometrie.

Um zum zwischenmenschlichen zurückzukehren, hinter jeder Junior-Wissenschaftlerin steht eine private Person und ohne mein Netz aus Familie und Freunden hätte ich den Durchblick und die Zuversicht nicht behalten können. Allen voran, das größte Dankeschön an meinen Bruder Marc, der wirklich immer Licht in den dunklen, langen Tunnel der Masterarbeit gebracht hat! Und natürlich DANKE Papa, you know, I couldn’t have done it without you!

Shoutout an Julia, auch wenn du die Arbeit niemals lesen wirst. Danke dir auch, für Alles!

Declaration

I declare that this thesis was composed by myself, that the work contained herein is my own, except where explicitly stated otherwise within the text, and that this thesis has not been submitted for any other degree or processional qualification except as specified.

I have tried to find all owners of the image rights and obtained their consent to use the images in this work. Should a copyright infringement become known, I request that you notify me.

Abstract

In order to gain more knowledge on the environmental behavior of thallium in As- and Tl-extreme environments, the abandoned As–Sb–Tl–Au Allchar deposit, North Macedonia with an exceptional mineral composition and high thallium grades of ore was chosen. This master thesis presents the results of a mineralogical investigation of solid waste dump material from the Crven Dol locality at the northern part of the deposit. To determine the retention of Tl by secondary minerals, X-ray fluorescence analysis (XRF), powder X-ray diffraction (PXRD), scanning electron microscopy with energy-dispersive spectroscopy (SEM-EDX) and Raman spectroscopy was used.

XRF showed that the mean concentrations of Tl and As in solid mining waste material and surrounding technosols are 3319 ppm and 58696 ppm, respectively, but can locally, in lorándite, $TlAsS_2$ and realgar-rich dumps, rise to extreme values of 10571 ppm for Tl and 165830 ppm for As.

PXRD analyzes revealed that the different solid waste samples are spanned mostly of carbonates (calcite and dolomite), quartz, gypsum, kaolinite-group minerals and muscovite, followed by orpiment, realgar, marcasite, pyrite, lorándite, and various calcium and iron arsenates. Due to the carbonate buffering, the acid mine drainage potential is low. Using SEM-EDX and Raman spectroscopy on polished sections, a closer look at the secondary minerals formed in the carbonate-buffered environments (pH = 7-8) was taken. Besides common arseniosiderite and/or yukonite, $Ca_2Fe_3^{3+}(AsO_4)_3O_2 \cdot 3H_2O$, talmessite $Ca_2Mg(AsO_4)_2 \cdot 2H_2O$, and minor thalliumpharmacosiderite, $TlFe_4(AsO_4)_3(OH)_4 \cdot 4H_2O$, the existence of small aggregates of at least five previously unknown secondary thallium-arsenate phases was proved. Furthermore, for the first time in Allchar deposit avicennite, Tl_2O_3 was reported on the weathered surface of a hand specimen.

This study provides further evidence of thallium uptake by newly found thallium secondary phases in carbonate-buffered, near-neutral As- and Tl-rich environments (Đorđević et al., 2021) and indicates the need for further studies on Tl speciation in As- and Tl-extreme environments.

Zusammenfassung

Um mehr Erkenntnisse über das Umweltverhalten von Thallium in As- und Tl- reichen extremen Umgebungen zu gewinnen, wurde die stillgelegte As-Sb-Tl-Au-Lagerstätte Allchar, Nordmazedonien mit ihrer einzigartigen mineralogischen Zusammensetzung und den hohen Thalliumwerten des Erzes ausgewählt. In dieser Masterarbeit werden die Ergebnisse einer mineralogischen Untersuchung von Haldenmaterial aus dem nördlichen Teil der Lagerstätte vorgestellt. Zur Bestimmung der Thallium-Sekundärmineralien der besonders Tl-reichen Lokalität Crven Dol im nördlichen Teil der Allchar-Lagerstätte wurden verschiedene analytische Methoden, wie Röntgenfluoreszenzanalyse (XRF), Röntgen-Pulverdiffraktometrie (PXRD), Rasterelektronenmikroskopie mit energiedispersiver Spektroskopie (SEM-EDX) und Ramanspektroskopie eingesetzt. Die Röntgenfluoreszenzanalyse ergab, dass die mittleren Konzentrationen von Tl und As in den Böden nahe der Deponien 3319 ppm bzw. 58696 ppm betragen, in lorándit- und realgarreichen Deponien jedoch lokal auf Extremwerte von 10571 ppm für Tl und 165830 ppm für As ansteigen können. PXRD-Untersuchungen zeigten, dass die verschiedenen festen Abfallproben hauptsächlich aus Karbonaten (Dolomit und Kalzit), Gips, Quarz, Muskovit, Mineralien der Kaolinitgruppe, gefolgt von Auripigment, Realgar, Pyrit, Markasit, Lorándit, $TlAsS_2$ und verschiedenen Eisen- und Kalziumarsenaten bestehen. Aufgrund dieser Karbonatpufferung ist das Risiko zur sauren Minenentwässerung glücklicherweise gering. Mittels SEM-EDX und Ramanspektroskopie an polierten Schliffen wurden die Sekundärminerale, die sich in den karbonatgepufferten Umgebungen (pH = 7-8) bilden, näher untersucht. Neben gewöhnlichem Arseniosiderit und/ oder Yukonit, $Ca_2Fe_3^{3+}(AsO_4)3O_2{\cdot}3H_2O$, Talmessit, $Ca_2Mg(AsO_4)_2{\cdot}2H_2O$ und geringem Thalliumpharmakosiderit $TlFe_4(AsO_4)_3(OH)_4{\cdot}4H_2O$ wurde die Existenz kleiner Aggregate von mindestens fünf bisher unbekannten sekundären Thalliumphasen nachgewiesen. Außerdem wurde in dieser Lagerstätte zum ersten Mal Avicennit an der verwitterten Oberfläche eines Handstückes nachgewiesen. Diese Studie liefert weitere Beweise für die Thalliumaufnahme durch neu entdeckte sekundäre Thalliumphasen in karbonatgepufferten, nahezu neutralen As- und Tl-reichen Umgebungen (Đorđević et al., 2021) und zeigt die Notwendigkeit weiterer Studien zur Tl-Aufnahme in As- und Tl- extremen Umgebungen.

List of abbreviations

Å	Ångström is a metric unit of length equal to 10^{-10} m
As	Arsenic
assd	Arseniosiderite
Au	Gold
cin	Cinnabar
fg	Fangite
gp	Gypsum
Hjrs	Hydroniumjarosite
Hpsd	Hydroniumpharmacosiderite
Kfs	Kalifeldspar
kln	Kaolinite-group
lor	Lorándite
MAC	Maximal allowable concentration
mm	Marcasite
mrc	Montmorillonite
phl	Phlogopite
Pmsd	Pharmacosiderite
ppm	Parts per million
PXRD	Powder X-ray diffraction
orp	Orpiment
Qz	Quartz
rlg	Realgar
Rt	Rutile
sco	Scorodite
Sb	Antimony
SEM	Scanning Electron Microscopy
SEM-EDX	SEM– Energy Dispersive X-ray
Tl	Thallium
tlm	Talmessite
Tpsd	Thalliumpharmacosiderite
U.S.	United States

USEPA	United States Environmental Protection Agency
WHO	World Health Organisation
XRF	X-ray fluorescence

Figures

Tables

Table of content

1 Introduction

Mining assures the supply of important resources of our daily life and is mandatory for our technological progress. At the same time, every mining project leads to various amounts of waste and to great pollution of the soils around and the groundwater. Mining is responsible for the loss of biodiversity as it implies the destruction of habitats. The enormous technological advance of our nowadays lives is highly depending on modern mining industries. They provide the world economy with a great diversity of mineral products which are used for various industrial and household purposes. With the exploitation of mineral resources, a huge waste problem accompanies as a result of removing large amounts of waste rocks in order to get access to the resource. The requested resource is often just components in a mass range of 100 per cent to a few ppm of the original resource (Lottermoser, 2010). An abandoned mine, and their inadequately dumped mine wastes, however, lead to several further environmental problems, such as contamination with toxic constituents, of the water table, rivers, and the surrounding soil. Leaving mine pits and any minerals to occur therein to weathering, results to the formation of secondary minerals. Per definition, secondary minerals, are those minerals which are formed during and-or through weathering. There is a difference between secondary minerals which are formed prior to mining by naturally processes and secondary minerals which are formed after the mining processes occurred. Sulfides for example, immediately start to weather when they are exposed to water and oxygen. As a consequence, contaminants could be more easily released (Lottermoser, 2010). There are many possible groups of secondary minerals that could form in this scenery, such as sulfates, oxides, hydroxides, carbonates, silicates and arsenates. Which types of secondary minerals are formed in the mine waste, is primarily dependent on the composition of the respective waste material and therefore the initial ore and the host rocks. These secondary minerals control the fate of metals and metalloids which were primarily formed by a chemical reaction with percolating rainwater. The fate of those metals and metalloids is regulated to that effect that those secondary mineral

phases incorporate or adsorb those contaminants. Hence the mineralogy of the secondary minerals dictates the fate of metals and metalloids and the solubility of these phases control the concentration of dissolved metals and metalloids. Thallium (Tl) and arsenic (As) for example quite often occur together and consequently also mobilize and scatter enormously into surrounding areas (Đorđević et al., 2021; Herrmann et al., 2018; Voegelin et al., 2015). As a result of that, secondary minerals matter in environmental mineralogy, as they function as a tool to immobilize ordinary toxic elements, e.g. thallium and arsenic, and act like a temporary or ultimate sink for those. For a better understanding of the immobilization and therefore of the incorporation through the secondary minerals, we want to study the weathering behavior of Tl and As.

Best place with regards to research the secondary mineralogy of those phases, is an environment with extreme values of these elements with little human impact, like the abandoned As-Sb-Tl-Au deposit of Allchar in North Macedonia and in particular, the northern part of the deposit, Crven Dol, with outstanding high values of Tl (Bačeva et al., 2014; Đorđević et al., 2021).

For this master's thesis, thallium and arsenic rich solid waste dump material and the surrounding technosol (the cover soil) from the Crven Dol locality, Allchar deposit, were investigated mineralogically, by using different analytical techniques (SEM-EDX, powder-XRD and X-ray fluorescence spectroscopy as well as Raman spectroscopy). In the solid waste dump material of Crven Dol extremely high values of Tl up to 10.5 g/kg and up to 166 g/kg of As (sample CD-3) were measured, which makes this locality a perfect natural laboratory for our research. Previous works on the petrology and age determination of Allchar deposit, have been published by Boev and Jelenković (2012) . Studies of the gold mineralization and a possible economic importance of the Allchar district was described by Percival and Radtke (1994) and later by Volkov et al. (2006). A comparison of the Allchar deposit with Carlin-type gold deposits was published by Palinkaš et al. (2018) and of course a very recent and ongoing study of the Tl and As retention in secondary minerals by Đorđević et al. (2021). There is a lack of sufficient investigations on the retention of Tl and As by secondary Tl and As minerals. The understanding of the mobilization of those secondary phases and their function to uptake toxic elements and in addition to it, in general, Tl speciation is the primary goal of this study.

As a result of this master thesis an update on secondary thallium mineralogy with at least five new thallium secondary phases in partly carbonate-buffered, near-neutral, As- and Tl-rich environments, is presented here. These phases were detected by SEM and were chemically characterized by the EDX at the present state of the research. The results prove that a monitoring of those extreme environments is indispensable and further studies on Tl speciation in high As- and Tl-environments and the mobility and stability of these secondary phases are needed.

As new findings of Tl-occurrences become more frequent in recent years, i.e. marine ferromanganese deposits (Manceau et al., 2022 and references therein) or soils of the Erzmatt locality near the village Buus in Switzerland (Herrmann et al., 2018) and furthermore findings of Tl-bearing minerals (Đorđević et al., 2021; Kasatkin et al., 2022; Gołębiowska et al., 2021) pile up, it stands to reason, that the risk of Tl exposure may be way higher than expected respectively than documented. Tl uptake by plants e.g. or a complete geochemical investigation of the groundwater at those sites could be an interesting investigation in future works.

2 Site description and geology

2.1 Site description

The abandoned Allchar deposit is a volcanogenic hydrothermal deposit, which is situated in the north-western margins of Mount Kožuf near the little village of Majdan (N 41°09'11.77", E 021°56'36.21"), a remote and quite harsh area in the southern zone of North Macedonia, about 110 km southeast of Skopje (Figure 1). Given its mineral composition it is besides Lengenbach deposit in Switzerland (Hofmann and Knill, 1996; Raber and Roth, 2018) and Langmuchang deposit in China (Xiao et al., 2004) one of the world most famous thallium deposits. Highly unique because of its outstanding high thallium grades of ore, especially in the Crven Dol locality (up to 10.5 g/kg) (this study, table 2) compared to its accumulation in the world. In Langmuchang, China, i.e., values up to 32-2600 mg/kg of Tl were detected in mining wastes (Xiao et al., 2004). These substantial thallium concentrations classify Crven Dol as a one of a kind deposit of this metal. The Allchar deposit is considered to be the first Carlin-type-gold deposit, which was found in the Balkan Peninsula in the mid 1980ies (Volkov et al., 2006; Boev and Jelenkovic, 2012). Furthermore, significant As (realgar) and Sb (stibnite) concentrations are economically interesting. An estimated amount of 15000 t As and 20000 t Sb remains in this locality (Volkov et al., 2006). In Allchar, gold mineralization was consistently investigated between 1986 and 1989. The exploration suggest that this deposit is similar to a Carlin-type gold mineralization like in the western United States, as measured by geochemical, geological, mineralogical and hydrothermal adjustments (Percival and Radtke, 1994). But there is one big difference compared to the Carlin-type gold deposits in the western part of the United States. The Allchar ore-deposit and its mineralization is not only hosted by sediments, but also by volcanics. The Kožuf district is a widespread volcanic complex, this region is part of the Vardar Zone and shares a frontier with Mount Kozjak. The complex has an east-west orientation and is about 30 km long. The east of the district is restricted by a fault zone and the western side is limited by a fault zone which separates the Vardar zone and the Pelagonian massif. The position of the volcanic complex in the transverse zone and the crossing with the Vardar zone, suggests a central type volcanism. This type of volcanism, which is activated on the tectonic intersection

which, on the other hand, is formed by a reactivated regional fault is characterized by ring-radial structures (Boev and Jelenkovic, 2012).
The volcanism here is tightly related to the Vardar zone in terms of its evolution and its genesis.

2.2 History of the Allchar Mine

Economical excavation of the ore body and their minerals started in the 19th century as Allchar became the most important As- source of the Ottoman Empire. It was also during the peak of mining, between 1881 and 1913, that Allchar got its nowadays name. Allchar is an abbreviation of the names Allatini - the proprietor of the concession, and Charteaux - a French mining engineer who conducted essential investigations at the deposit (Boev and Jelenkovic, 2012). Before that, it was known as Kožuf. During that period of the first economic exploitation, As-Sb ore was mined and exported to Germany, particularly to Freiberg. It was also in the smelter of Freiberg back then, when high contents of Tl-minerals like vrbaite, $Hg_3Tl_4As_8Sb_2S_{20}$ (Jezek, 1912) and lorándite, $TlAsS_2$ (Krenner, 1897) were identified (Volkov et al., 2006). Though, no information is left on the quantity of the mined ore that time. Arsenic reserves nowadays, however, are amounted to be at roughly 15.000 t (Boev et al., 2001). This element is considered to be an unwantedly admixture of antimony concentrate (Volkov et al., 2006). But then again, economic exploitation of Sb ore was precluded due to that high arsenic contents in antimony concentrates (Jankovic and Jelenkovic, 1994). There was a great survey on the whole Sb mineralization after World War II from 1958 to 1974. It is estimated that Sb reserves exceed 20.000 t in Allchar, with a mean Sb grade of 0.5 % (Boev et al., 2001). The latest exploration of this deposit was in the 1980's, when the industry became interested in thallium for solar neutrino sensors (Amthauer et al., 2012). It was mainly exploited in the northern zone of the deposit, known as Crven Dol (Boev et al., 2001; Volkov et al., 2006). It is assumed that the thallium reserves are about 500 t, which makes this a large deposit of thallium, and a medium deposit regarding to gold and antimony reserves (Volkov et al., 2006). Percival et al. (1990) reported a large Au anomaly in the southern and central part of the deposit (Percival and Radtke, 1994). Nevertheless centuries of mining and a complex geology lead to an enrichment of toxic elements at Allchar area (Đorđević et al., 2021).

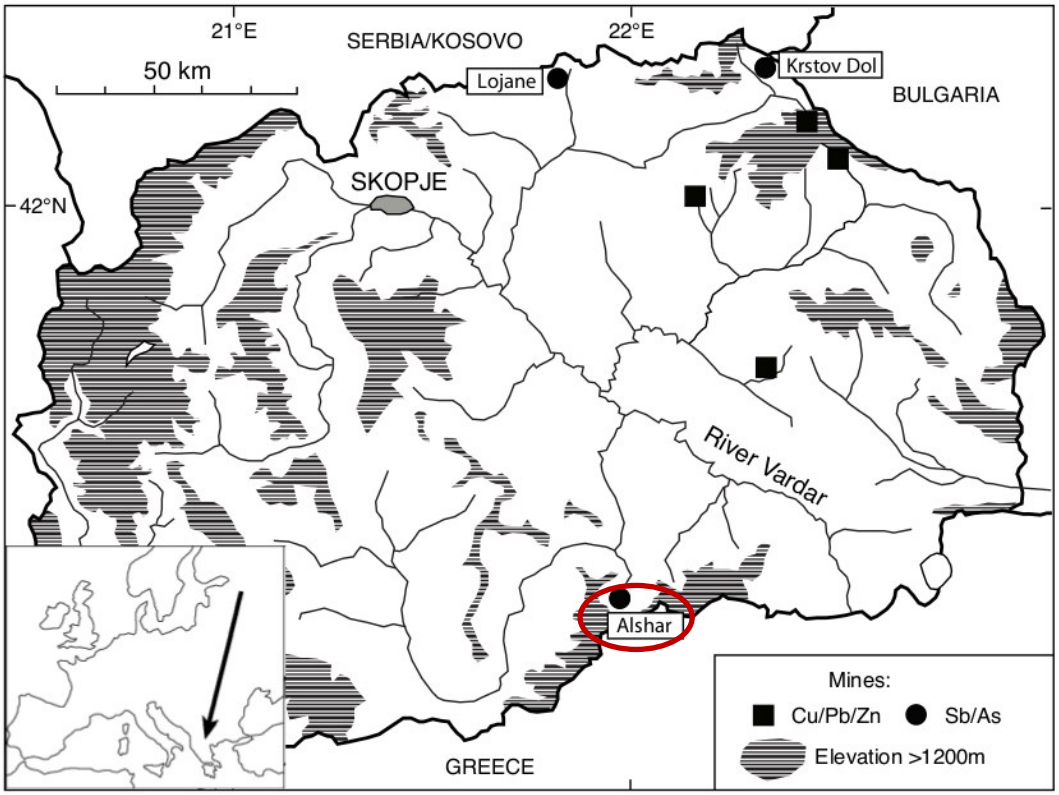

Figure 1: Map of North Macedonia with Allchar locality marked in red (Alderton et al., 2014)

2.3 Geology

The Allchar region is composed of several geological formations, spread in different stratigraphic complexes. There is a complex of Precambrian metamorphic rocks, a complex of metamorphic Paleozoic rocks, a complex of sedimentary rocks from Triassic-Jurassic era , a sedimentary rocks complex of Upper-Cretaceous, a complex of Upper-Eocene rocks, a complex of Pliocene sediments and pyroclasts and a complex of Quaternary sediments (Boev and Jelenkovic, 2012). This initial situation, of a Pliocene volcanic mineralization and Triassic carbonate host rocks like marble and dolomite which are again overlain by tuffs and dolomites as a Tertiary volcano-sedimentary sequence, combined with centuries of anthropogenic mining, lead to this special enrichment of toxic elements (Tl, As) in the Allchar area (Đorđević et al.,

2021). The Allchar deposit contains mainly of Fe, As, Sb and Tl, which are followed by low Au, Hg and Ba as well as traces of Cu, Pb and Zn. Pyrite, marcasite, realgar, orpiment and stibnite are the prime minerals of the deposit along by a gangue of dolomite or finely grained quartz. There are three, not directly defined zones, where different mineralization took place (Janković and Jelenković, 1994) see Figure 2:

(I) the northern part, with a dominance of As and Tl mineralization together with low Sb and locally traces of Au and Hg. Crven Dol belongs to this northern part of the deposit

(II) the central part, dominated by Au and Sb, accompanied by Tl and As, minor Ba and Hg as well as traces of Pb

(III) the southern part, the high-temperature zone, with a dominance mineralization of Au, along with divergent As and Sb

The main ore minerals of Crven Dol locality are realgar As_4S_4, pyrite/marcasite FeS_2 and orpiment As_2S_3. The interesting part of Crven Dol shows several rare thallium minerals, such as the scientific relevant thallium arsenic sulfosalt named lorándite $TlAsS_2$, which is used as a detector of solar neutrinos through a special nuclear reaction involving thallium (Amthauer et al., 2012). Especially the secondary mineralogy of this deposit is far from being fully studied. Nevertheless nine new thallium minerals were discovered in this ore deposit: bernadite* $TlAs_5S_8$, dorallcharite* $TlFe^{3+}{}_3(SO_4)_2(OH)_6$, jankovićite* $Tl_5Sb_9(As,Sb)_4S_{22}$, lorándite* $TlAsS_2$, parapierrotite* $TlSb_5S_8$, picotpaulite* $TlFe_2S_3$, raguinite* $TlFeS_2$, simonite* $TlHgAs_3S$ and vrbaite* $Hg_3Tl_4As_8Sb_2S_{20}$ (Cvetković et al., 1995; Pavićević and El Goresy, 1988). Allchar is the type locality for those minerals mentioned and marked with * above. A full review on the mineralogy of Allchar deposit were given by Rieck and Boev et al. (Rieck, 1993; Boev and Jelenković, 2012).

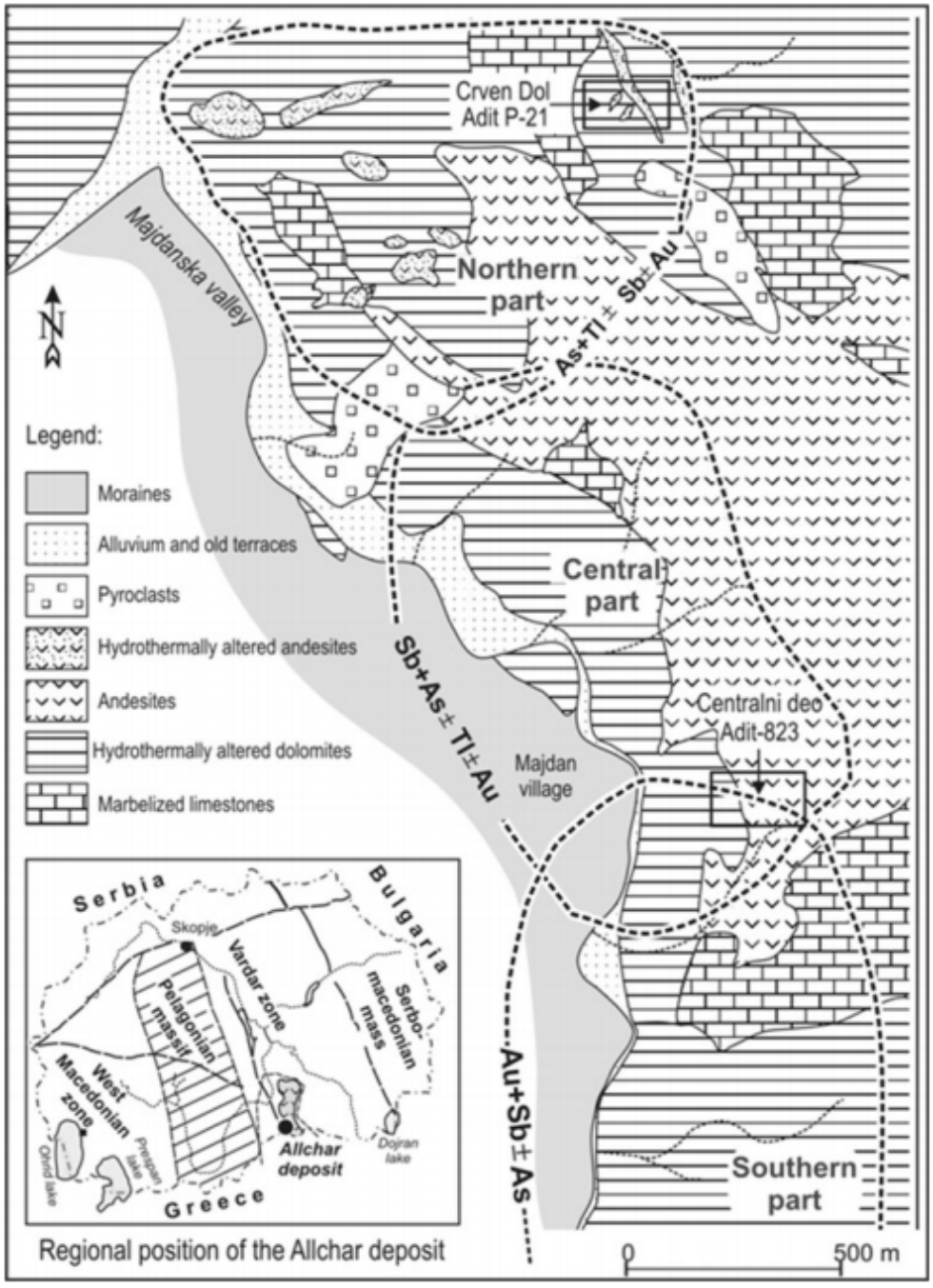

Figure 2: Regional position of the Allchar deposit

3 Geochemistry and mineralogy of the contaminants

3.1 Thallium

In 1861 independently discovered by William Crookes and Claude Auguste Lamy, thallium (Tl) is considered to be a “heavy metal” due to its high density (11.83 g/cm^3) (Peter and Viraraghavan, 2005). It appears in the oxidation state I and III. Independently of the oxidation state of thallium, most of its complexes are highly toxic, more toxic than arsenic, lead or mercury compounds. When exposed to soluble Tl salts, the lethal dose for human lies within 10-15 mg/kg (Chen et al., 2019). The main anthropogenic reason why Tl occurs in nature is because of mining of sulfidic minerals, metal smelting, coal combusting and mine drainage. In the last decades, thallium has been widely used in aerospace, chemical industry and electronics. Another promising application of thallium is optical fiber catalyst and superconducting material (Peter and Viraraghavan, 2005). This highly toxic element is prevalently hosted by sulfides and sulfosalts in combination with low-temperature hydrothermal mineralization. Another appearance of thallium in nature is by incorporating into secondary sulphate minerals, where they operate as temporary reservoirs for thallium. There are 84 minerals which are recognised by the IMA (International Mineralogical Association) that include essential Tl (IMA 2022). Even though its abundance is very low in soil, water, sediments and most other natural habitats, Tl is listed by the USEPA (United States Environmental Protection Agency) as a priority pollutant. Tl(I) shows both lithophile and chalcophile character, ergo small amounts of Tl(I) can be found in metal sulfides such as pyrite, marcasite, sphalerite, galena, stibnite, realgar and in sulfosalts. Tl also occurs in sulfosalts and sulfides of Pb^{2+} and Ag^{+} because of the similarity of the ionic radii of Pb^{2+}, Ag^{+} and Tl^{+} (Zhao and Gu, 2021). Based on the same charge and a similar ionic radius Tl^{+} easily substitutes with K^{+} (1.70 Å for Tl^{+} and 1.64 Å for K^{+}). By this isomorphic substitution, Tl can be incorporated into K-bearing silicate minerals such as K-feldspars and micas.

Consequently Tl is able to form independent sulfides and it typically appears in the sulfosalt minerals with Zn, Pb, Cu, As, Fe, Sb, Hg and Au in diverse hydrothermal processes (Xiong, 2009). Similar to alkali cations, Tl(I), as well is very soluble, bioavailable and mobile. As a result of this, in aquatic environments with general low Tl concentrations, Tl(I) has a disposition to dominate over Tl(III). Another reason for the dominance of Tl(I) compared to Tl(III), even though the toxicity of Tl(III) is way higher than that of Tl(I), is, that Tl(I) is far more thermodynamic stable than Tl(III) (Zhuang et al., 2021). Also, Tl(III) can be reduced to Tl(I) or alternatively form insoluble hydroxides. To stabilize the soluble Tl(I) it is necessary to form complexes with sulfate, carbonate, chlorite, nitrate and organic matter. That's the reason for more mobility and bioavailability of Tl(I) than of Tl(III) (Xiong, 2009).

3.2 Arsenic

Arsenic (As) is a chalcophile chemical element which is considered to be a metalloid and appears in several oxidation states: -III, -I, 0, III, V. Arsenic causes serious damage to human health and the environment, consequently As is considered to be one of the most toxic elements (Nordstrom, 2002). The lethal dose of arsenic to humans is approximately between 1-3 mg/kg/day (ATSDR, 2007). Once incorporated in the human body, arsenate e.g. enters via the phosphate transporters and arsenite enters via the aquaglyceroporin channels, it can substitute beneficial nutrients (Bowell et al., 2014). Arsenic containing compounds are proven to be carcinogenic to human (McCarty et al., 2011), hence the maximum tolerated doses was stated by the World Health Organization (WHO) 2017, with 10 µg/l for drinking water. Widely distributed in the environment, arsenic is concentrated by hydrothermal and magmatic processes in the earth's crust and was primarily used as a "pathfinder" for metallic ore deposits especially gold, copper, tin and tungsten (Bowell et al., 2014). As-containing minerals include mostly arsenates (approximately 60% of the As-bearing minerals), sulfides and sulfosalts, arsenites and oxides, arsenides and elemental arsenic. Especially high concentrations of arsenic can be found in many hydrous metal oxides and oxide minerals either as sorbed and occludes species or as part of their periodic structure (Bowell et al., 2014). When arsenic is bound to oxygen and sulfur, which happens most commonly, it occurs in the III (arsenite) and V (arsenate) oxidation states (Herath et al., 2016). Particularly well known to accumulate As are iron oxides, with

concentrations up to several weight per cent. Arsenic with an atomic radius of 1.15 Å and an oxidation state of either III or V can substitute for P (V with 0.98 Å), Si (IV with 1.10 Å), Al(III with 1.25 Å), Fe (III with 1.40 Å) and Ti (IV with also 1.40 Å) in several mineral structures although at much lower concentrations (Bowell et al., 2014). Hence arsenic is present in many petrogenic minerals. Primarily arsenic is concentrated in sulfide minerals where it can occur as either an arsenide or a sulfoarsenide, functioning as an anion bond to transition metals (e.g. arsenopyrite FeAsS). More rarely, but also possible, the element is concentrated in mineral phases where As forms nominally a cation like in realgar, AsS and orpiment As_2S_3 (Bowell et al., 2014). These native arsenic bearing arsenides and sulfoarsenides are the most common primary arsenic minerals in mining affected environments. In addition to that, a huge number of secondary As bearing mineral phases can be found in those environments, generally in extremely contaminated soils, previous industrial sites and stream sediments (Drahota and Filippi, 2009). These secondary arsenic oxides and oxysalts are formed by altering of primary As-minerals in ore production but also by weathering of those. Contrary to a lot of metals, the mobility of arsenic is only increasing under neutral to high alkaline pH and also under strong acidic conditions. Beside, arsenic can be mobile in quite oxidized and reduced waters (Craw and Bowell, 2014). Predominantly arsenic exists under reducing conditions as As(III) and under oxidizing circumstances, it appears as the less mobile As(V) (Herath et al., 2016). Arsenite, because it sorbs stronger onto surfaces of minerals, is ten times more toxic and mobile than the aqueous arsenate (Larios et al., 2012).

3.3 Antimony

Antimony (Sb) occurs in three common oxidation states -III, +III, +V in nature (Bowell et al., 2014). They vary in their toxicity, the Sb(III) species are ten times more toxic than the Sb(V) species. When Sb forms inorganic compounds, they are more toxic and also more likely to occur than organic compounds. Nevertheless, elemental antimony is the most toxic one (Smichowski, 2008). It is a genotoxic element with quite harmful effects on humans (Herath et al., 2016). The human heart is quite sensitive to Sb, but also the gastrointestinal and the respiratory tract, in addition to that it is considered to be carcinogen. When contaminated with Sb, it is admittedly

poorly absorbed and not metabolized but spread throughout the body. When the oral uptake of Sb(III) exceeds 1 mg/kg/day toxic adverse effects are to be expected (ATSDR, 2019). Therefore, the threshold for antimony in drinking water is determined by the World Health Organization at 20 µg/L (WHO, 2017 and references therein). Sb is a chalcophile, silver metalloid, which coexists with many other metalloids or metals such as Cu, Hg, Ba, Ag, Au, Zn, Pb, P, S, Ni, Co, Fe and of course and especially with As. Based on the latest standards and according to the contiguity to arsenic in the periodic table, Sb is often related to As (Herath et al., 2016), however antimony is not as well-studied as arsenic. Apart from this close connection, the larger cation radius of Sb leads to different sorption sites or host phases (Courtin-Nomade et al., 2012) Sb(V) is predominant, thermodynamically more stable and more mobile than Sb(III), on oxidizing and mildly reducing conditions.

Antimony is mostly mined from hydrothermal ores (Roper et al., 2012). Sulfides do dominate its primary mineralogy, as it is a chalcophile element. The economically most important Sb-mineral is stibnite Sb_2S_3 (Multani et al., 2016). Other Sb-sulfides to be mentioned are the members of the tetrahedrite-tennantite series (Roper et al., 2012). Antimony sulfides dissolve if exposed to oxygen and release the containing elements, just like other sulfides (Lottermoser, 2010). This leads to the precipitation of secondary phases. Mainly oxides are formed as those secondary Sb-minerals, following a precise oxidation sequence, as such: stibnite → kermesite, Sb_2S_2O → senarmontite/valentinite, Sb_2O_3 → cervantite, $Sb^{3+}Sb^{5+}O_4$ → roméite-group antimonates (RGA) (Roper et al., 2012).

4 Sampling and sample preparation

4.1 Sampling

The samples analyzed for this master's thesis were collected at four different waste dumps with joint soil outcrops. These four locations are within a distance of 150 m of each other (N 41°09'33.80"; E 21°57'06.20" are the average GPS coordinates). Near to the entrance of the Adit 21, two semi profiles were (sample CD-1 and CD-2) dug out. There is a surrounding of yellowish gray, porous but also fine-grained mine dump material. The waste dump, where sample CD-3 was gathered, was quite condensed and strongly weathered. Also, it was overgrown by a fine layer of mosses. The entrance of the Adit 21 is only about 50 m uphill from the waste dump number three, where also hand samples were taken which were analyzed during this study. The hand specimens (CD3-HS, CD3A-HS and CD3A2-HS) were collected at this realgar-rich and lorándite-bearing, strongly weathered and compacted waste dump. For a full description of the sample collection see Đorđević et al., 2021. A total of 9 samples from this locality with clearly visible effects of weathering were collected. All samples were examined in order to obtain general information about petrography of original rocks, primary ore assemblages and minerals of the presumed supergene origin. After screening based on the presence of primary sulfides and dominant minerals, four representative samples were studied in detail. These samples represent crusts (CD3-HS, CD3A-HS and CD3A2-HS) and individual crystals, as well as polished sections (three) which were either physically removed from the surface of mineralized rocks or were cut out and polished for further investigations. The crusts were analyzed by powder X-ray diffraction (PXRD) and the polished sections measured with SEM-EDX and micro-Raman spectroscopy. The fourth sample (CD-4) was composed from an excavation hole, which was dug out from the technosol of the streamlet bed, about 30 m along downhill from the third site. Also, here hand specimens were composed. For sufficient analyze possibilities, 25 kg material were taken approximately from each site or hole.

4.2 Sample preparation

For different analyze methods, different sample preparations were necessary. Firstly, samples CD1 to CD-4 were divided with a sample splitter into two equal fractions. Subsequently one half of the dry material was sieved to the ≤ 2 mm fraction (Figure 3). This fraction was processed into homogenized rock powder, which is required for XRF and PXRD measurements, where rock powder pellets (Appendix 8) were compounded. To produce the powder, the sequence of ≤ 2 mm were initially broken down to a smaller grain size using a jawbreaker. Afterwards, this material was milled down to an utterly homogenized rock powder by using a swing mill. To avoid contamination of the samples, it was necessary to use a mill which is harder than the raw material. In this case an agate mill was used. To receive a powdered material with a grain size of approximately 30-35 µm it takes about ten minutes in the refiner. This procedure was done after (Nagl and Mader, 2019). For SEM-EDX and Raman spectroscopy polished sections were prepared (Appendix 9). Therefore, the other half of the sieved ≤ 2 mm fraction was used. Chosen pieces were embedded in resin and polished with corundum. The sample surfaces need to be carbon-coated before SEM-EDX measurements are possible, to get a thin conductive layer which inhibits charging.

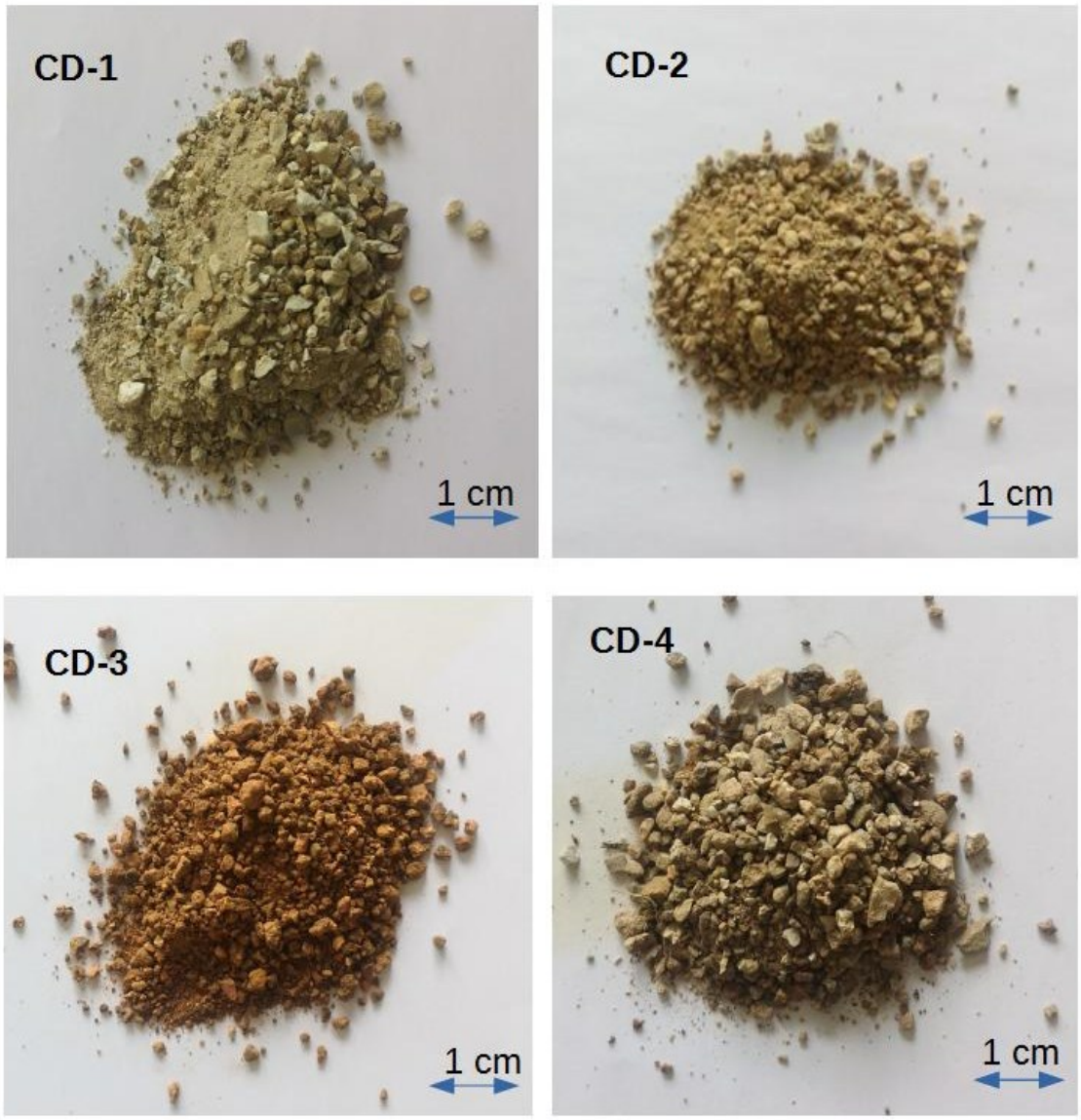

Figure 3: Raw samples CD 1-4

5 Methodology

5.1 X-Ray fluorescence spectroscopy (XRF)

X-ray fluorescence analysis is a powerful, non-destructive method for a quick and quantitative analyze of all elements with an atomic number above oxygen (> eight) (Skoog et al., 2013). This method gives a quantitative proof of existent elements of the sample as well as a qualitative element analysis.

A XRF-instrument generates an X-ray beam by an X-ray tube, with enough energy to excite the inner shell electrons of the investigated elements. If the binding energy is less than the beam energy, the X-ray beam leads to a displacement of the electrons. When, in the sample, the X-ray hits an atom, it becomes excited or ionized. Consequently, the atom ejects an inner shell electron and subsequently an electron from the outer-shell fills the gap by dropping down. This very movement emits fluorescence radiation, emitted as a secondary X-ray, which is measured by the detector. The energy of the radiation equals the energy difference between the two electron shells. That difference is unique for each element and enables to identify every element by its characteristic florescence radiation in an energy dispersive XRF-instrument (Skoog et al., 2013).

There are different spectrometers, depending on the detector. The X-rays could be separated as per their element specific wavelength (wavelength dispersive X-ray fluorescence spectrometry, WDX) or as per element-specific energy (energy dispersive X-ray fluorescence spectrometry, EDX). EDX is not as accurate as WDX but therefore cheaper, less fault-prone and faster (Skoog et al., 2013).

A detailed instruction for the sample preparation, quantification and measuring procedure is described by (Nagl and Mader, 2019). Approximately 10 g of the homogenized rock powder and 0.5 ml of aqueous polyvinyl alcohol, as a binding agent, are manually mixed well for 10 minutes. Using a hydraulic press by reaching a pressure of 16 T/cm^2, this mixture is pressed to pellets (Appendix 8). Before the analyze could start, the pellets need to dry overnight in an oven at 70 °C.

The XRF analyzes are performed on a sequential X-Ray spectrometer PHILIPS PW2404 with a super-sharp end-window tube with a Rh-anode and a programmable 4 kW generator (60 kV max., 125 mA max.; iso-Wattswitching), the accompanying

software is PANalytical "SuperQ" vers. 5.1B (5.2822.3) with the options "Pro-Trace" and "Omnian" (Nagl and Mader, 2019). These two different software modules, “Pro Trace” and “Omnian”, which are utilized by the Department of lithospheric research at University of Vienna, were used for this study, to analyze the data. Pro Trace works with specific standards and allows an accurate measurement of trace elements concentrations. Whereas Omnian provides a convenient and rapid quantitative analysis of major and trace elements without any standards. Omnian is based on a fundamental parameter calculation (Nagl and Mader, 2019).

5.2 Powder X-Ray diffraction (PXRD)

Powder X-ray diffraction is one of the most important tools to identify and quantify different phases in crystalline materials. It can also provide crystallographic information (unit-cell dimensions, crystal structure) and quantitative information about a sample. A powder X-ray diffractometer nowadays is composed of an X-ray generator, an X-ray tube, as well as a sample holder and a detector. It is based on a constructive interference of monochromatic X-rays and a crystalline sample. A cathode ray tube is generating those X-rays, which are filtered to create monochromatic radiation and bundled to concentrate all to be targeted towards the sample. When the conditions underlie Bragg`s Law ($n\lambda=2d \sin \theta$) the correlation of the incident rays together with the sample create constructive interference as well as a diffracted ray. Bragg`s law is bringing the wavelength of electromagnetic radiation of the diffraction angle in connection with the lattice space of a crystalline sample. These X-rays which are diffracted can be detected, counted and processed. The diffractometer works with a Bragg-Brentano theta-2theta configuration, with a tilted sample compared to the primary X-ray beam by an angle theta. The reflected as well as the incident beam have the same angle compared to the surface of the sample. With the velocity ω, the sample is being twisted around the goniometer axis, whereas the moving of the detector is $2\,\omega$ (Allmann, 2003; Spieß et al., 2019). Based on the arbitrary orientation of the powdered material and the scanning through the range of 2θangles all the conceivable diffraction directions of the lattice should be accomplished. The basic principle of PXRD is that diffraction appears when light is being dispersed by a periodic arrangement with a long-range order and therefor

constructive interferences with a precise angle are being produced. In each atom all the electrons coherently scatter light. With which strength the atom disperses the light is proportionally connected to how many electrons are around the atom. According to the periodic arrangement of atoms in a crystal in all three dimensions, the light is being diffracted. As the wavelength of the X-rays are similar to the atomic distances the elastic scattering, which is produced when the X-rays hit an atom, it interferes in crystal specific direction with the electrons, without losing energy. This scattering however produces a diffraction pattern which is very specific and contains information about the periodic order within the crystal. Each diffraction pattern is impacted by the unique crystal structure of a material. We get a diffractogram of the angle theta plotted against the intensity and therefor a lot of information about the sample material. The different peaks can determine the phase composition, a phase analysis (quantitative), the unit cell lattice parameters, the crystal structures and the mean crystallite size. There are databases available, such as the Powder Diffraction File (PDF) of the International Centre for Diffraction Data (ICDD), to compare the experimental data to thousands of reference diffraction patters to determine what phases are present in the sample (Spieß et al., 2019). The sample is about 3g of homogenized rock powder, which contains ten thousands of randomly oriented crystallites, pressed and therefor flattened in a Si sample holder (Appendix 10b).

A Bruker D8 Advance diffractometer (Appendix 10a) was used for the analyzes of the samples at the Institute of Mineralogy and Crystallography of the University of Vienna under the following conditions: CuKα radiation, position-sensitive Lynxeye detector. The excitation voltage and the electric current are 40 kV and 25 mA for the diffractometer. The measurement range was between 5 to 85° 2θ at room temperature with a step size of 0.018° 2θ and a dwell of 1s per step. To identify the peaks and the phases DIFFRAC.EVA software, version 4.2, and the ICDD powder diffraction file PDF-2 was used.

5.3 Scanning electron microscope with energy-dispersive X-Ray spectroscopy (SEM-EDX)

The scanning electron microscopy is a frequently used method to study organic and inorganic materials from a micrometer (µm) to a nanometer (nm) scale. The benefits

of this imaging instrument are high spatial resolutions, a simple preparation of the specimen and an overall large depth of field. Especially in mineralogy, SEM is appreciated for its images to study the morphology of crystals on a microscale. The contained Energy Dispersive X-ray Spectrometer allows chemical composition analyzes. It is possible to detect elements with an atomic number ≥ eight (oxygen). Depending on the detector nowadays it is even possible to analyze elements of an atomic number starting from four.

A control console as well as an electron column are the two prime components of a SEM. This electron column is composed of an electron gun and at least two electron lenses. Those lenses operate the paths of electrons while traveling down an air-evacuated tube. The vacuum which is produced by vacuum pumps is about 10^{-4} Pa. The electrons generated with an electron gun accelerate with an energy in the range of 0.1-30 keV and form an electron beam. With this electron beam it is possible to either form an image of the sample by scanning the surface, or to identify and analyze one specific point of the sample. As there is interaction between the secondary electrons of the sample and the electron beam, it leads to backscattered electrons and characteristic X-rays. These interactions are the major signals used to form a high-resolution image. By scanning the sample line by line, an image is formed one point after another. All those signals are received by a detector, intensified and visualized by the control console, the computer. The pixels of the formed image appear lighter or darker, depending on how intense the received signal is. With analyzing the specific X-rays which are emitted by the sample it is feasible to get elemental information plus qualitative and semiquantitative identifications (Goldstein et al., 2003).

As part of this master thesis the measurements of the chemical compositions of the individual mineral grains, as well as their images were collected using a JEOL JSM-6610 LV scanning electron microscope (SEM) equipped with an energy-dispersive X-ray (EDX) detector (Bruker e$^-$Flash HR, resolution of 127eV) and Bruker Esprit 2.0 software (Natural History Museum, Vienna). The excitation voltage of 15 kV was used. The samples were previously coated with carbon to avoid overcharges on the surface (see Appendix 9).

5.4 Raman spectroscopy

The Raman spectroscopy allows an identification of minerals even in small grain sizes (not larger than a few millimeters) or xenomorphic crystals. This methodology is a non-destructive and fast way of sample analyzing, allowing also the distinction of isochemical polymorph phases (Nasdala and Schmidt, 2020). Furthermore, it is possible to analyze unprepared samples, for this study however only polished samples were used. The way this spectroscopy method works is a so-called scattering phenomenon in which the used photons interact with the covalent bonds of the solid particles of the sample. Thereby photons are scattered back in an inelastic way and with this the lose energy the Raman shift is produced. The described shifts reflect the vibration energy which occurs between the bonded atoms of a molecule within the sample. The scattering phenomenon can be divided into two different types of scattering. One, being the so-called Stokes scattering, which defines an energy loss due to the fact that the molecule has a higher vibrational state than before the excitation. The opposite effect to this is the Anti-Stokes scattering, the second type of scattering, where the molecule has a lower vibrational state than before the excitation. The differences within those energy levels compared to the exciting photons equals the energy differences between the vibrational states of the molecule. The Raman shift itself is plotted against the intensity, showing phase characteristic peaks. Therefore, only single molecular units and no single elements can be measured.

For this master thesis, Raman spectra of the polished sections (embedded in resin, Appendix 9) were measured with a Horiba LabRam-HR system equipped with an Olympus BX41 optical microscope in a spectral range between 100 to 4000 cm^{-1}, at the Institute of Mineralogy and Crystallography of the University of Vienna. The 632.8 nm excitation line of a He-Ne laser was focused with a 50x or 100x objective (N.A. = 0.90) on the randomly oriented crystals and crystalline aggregates. The spectra were acquired with a nominal exposure between 10 and 120 s (confocal mode, 1800 lines/mm, 1.5 µm lateral resolution, and approximately 3 µm depth resolution). The laser power density was adjusted on the mineral measured to avoid possible sample changes due to intense laser-light absorption and originating temperature increase.

6 Results

6.1 Chemistry of the bulk samples

Figure 3 shows a picture of the raw samples, sieved to the ≤ 2 mm fraction. This material is than processed into homogenized rock powder for the XRF analysis (Chapter 5.1). The concentrations of the major elements measured as oxides are given in Table 1. The most common oxide in all samples is CaO. It dominates in all samples except in in CD-4, where the major oxide is SiO_2. Its amount of 27 wt.% is noteworthy since it is the highest SiO_2 value measured in all four waste dump samples. The second most common oxide is therefore SiO_2, followed by MgO. The third sample however shows the highest value of Fe_2O_3 with outstanding 37 wt.%. This value is also the highest measured one in all four samples. Sample CD-4 shows the highest value of Al_2O_3 with 8.6 wt.% and the second highest value of Fe_2O_3 with 12 wt.%. The high CaO values in all four samples proof the presence of carbonate rocks in the waste material.

The relevant trace elements measured in ppm of each sample are given in Table 2. A list of all measured trace elements is given in Appendix 5. Sample CD-1 shows the lowest value of As with approximately 16860 ppm, whereas it shows the highest Sb values of 110 ppm. In sample CD-3 the highest concentration of thallium (10571 ppm) was measured. Considering amounts like 16860 ppm of arsenic, it is rather not a matter of trace elements.

Table 1: Total concentration* of major oxides measured by XRF in wt.%

Major Oxides	CD-1	CD-2	CD-3	CD-4
	[wt%]	[wt%]	[wt%]	[wt%]
CaO	33.00	23.00	4.90	18.00
SiO_2	9.30	10.00	2.90	27.00
MgO	8.30	10.00	0	4.50
TiO_2	0.11	0.12	0.03	0.30
Al_2O_3	3.50	4.20	1.40	8.60
Fe_2O_3	1.90	6.30	37.00	12.00
MnO	0.18	0.48	0.26	1.30
Na_2O	0.07	0.11	0.08	0.89
K_2O	0.37	0.56	0.16	1.70
P_2O_5	0.047	0.11	0.22	0.23
H_2O	40.54	35.69	25.44	21.37
sum	97.32	90.57	72.39	95.89
F	0	0.19	0	0.18
SO_3	1.00	6.00	14.00	1.50
Cl	0.0085	0.0088	0	0.01
MJ total	98.33	96.76	86.39	97.58

* *values rounded to two significant decimals*

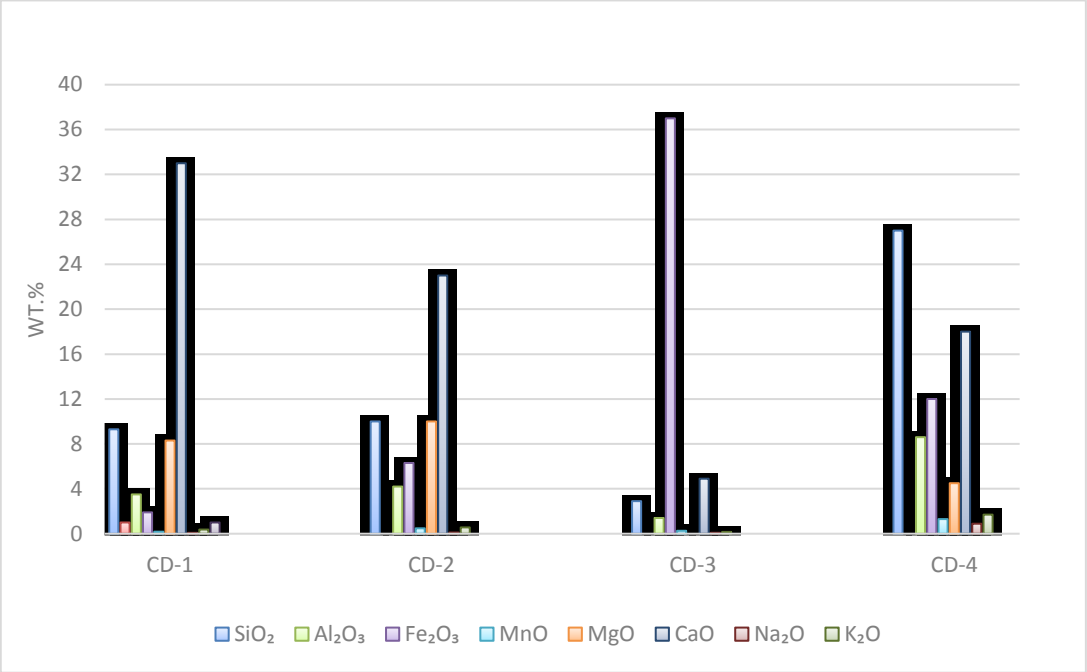

Figure 4: Concentration of major oxides (XRF)

Table 2: Total concentration* of significant trace elements measured by XRF

Element	CD-1 [ppm]	CD-2 [ppm]	CD-3 [ppm]	CD-4 [ppm]
As	16,855.10	30,690.30	165,830.70	21,405.90
Tl	979.50	969.00	10,571.20	755.20
Sb	110.80	10.20	10.10	20.00
Fe	13,200.00	43,900.00	258,000.00	84,000.00

**values rounded to two significant decimals*

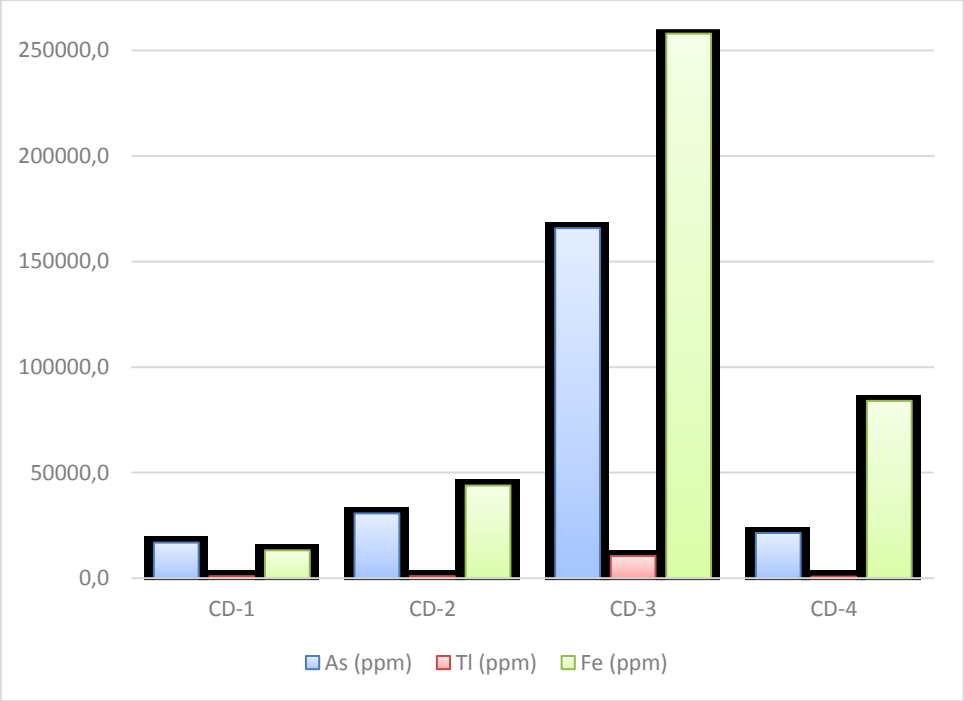

Figure 5: Trace elements chemistry measured by XRF

6.2 Mineralogy of the samples

6.2.1 General mineralogy

The analyzes of the bulk samples showed that the most abundant ore minerals of the waste dump samples are realgar and orpiment, followed by minor lorándite, pyrite and marcasite mixed with a gangue of quartz, calcite, dolomite, goethite, barite and gypsum, depending on the single sample (Figure 6). As most frequent secondary minerals, Fe-oxides and Fe-oxy-hydroxides (FOH´s), Ca-arsenates (arseniosiderite and yukonite) and Mn-oxides should be named, followed by Ca-Mn-arsenates, newly discovered Tl-metal-arsenates and talmessite (Tables 3-6). The colour of the powdered samples varies between light yellow to grey-brownish, beside sample CD-3 where the colour is a bright brown orange, due to its high realgar content (see Table 3) It is also sample CD-3 where the dominant minerals differ from the others, here there are no carbonate minerals present. Dolomite and calcite are the most abundant carbonates in the other three samples (Figure 6). Also, the primary ore minerals differ in sample CD-3 where lorándite and realgar are the most abundant ones. As for the secondary phases, the hand samples CD3-HS, CD3A-HS and CD3A2-HS show some differences to the others. These are the only samples where neither Mn-oxides nor Ca-Mn-arsenates were found. Their PXRD analyzes (Figure 8), where the surface was scratched and powdered, showed that gypsum was the most abundant mineral, followed by quartz, kaolinite and muscovite. Realgar is the most frequent ore mineral in these samples and is also easily identifiable through a binocular microscope. In the hand specimen CD-4HS, the primary ore minerals are like in sample CD-2, mostly pyrite, marcasite, orpiment and fangite (in order of quantity). The dominant minerals of this sample are dolomite, calcite, K-Na-feldspars and quartz, as well as muscovite, barite and kaolinite. It is also sample CD-4HS where up to five new Tl-arsenate phases were found. For a better identification on the most of all very tiny secondary phases of the samples (predominantly <20 µm, in some cases even <5 µm) a combination of SEM-EDX and Raman spectroscopy was used. Using PXRD a good overview of the main (dominant) crystalline minerals were given. However for the identification of the amorphous phases and the less abundant minerals, SEM-EDX and Raman spectroscopy were used on the polished samples (Table 3 Appendix 9).

Table 3: Description of the studied samples including the hand specimens (HS)

Samples	Color powder	Dominant minerals	Primary minerals	Secondary phases
CD-1	Light-toned greyish yellow	Calcite, dolomite, quartz, muscovite, kaolinite,	Orpiment	FOHs, talmessite
CD-2	Light-toned brownish orange	Dolomite, gypsum, quartz, muscovite, kaolinite	Pyrite, marcasite, orpiment	FOHs, arseniodsiderite
CD-3	Bright orange brown	Gypsum, quartz, Muscovite, kaolinite	Lorándite, realgar	FOHs, dorallcharite, jarosite, hydroniumjarosite, scorodite, Tl-bearing pharmacosiderite, natropharmacosiderite, hydroniumpharmacosiderite
CD-4	Light-toned brownish-grey	Dolomite, calcite, muscovite, quartz, kaolinite	realgar, orpiment	FOHs, dorallcharite, montmorillonite
CD3-HS	Orange-greyish	Gypsum, kaolinite, quartz	realgar	Dorallcharite, pharmacosiderite, avicennite, FOHs, Tl-pharmacosiderite
CD-3AHS	Bright orange brown	Gypsum, muscovite, quartz	realgar	Dorallcharite, pharmacosiderite, Hydroniumjarosite, FOHs
CD-3A2HS	Light brown greyish	Gypsum, quartz	realgar	Dorallcharite, pharmacosiderite, hydroniumjarosite

CD4-HS	Light-grey to brownish	Dolomite, gypsum	Pyrite, lorándite	Arseniosiderite, Ca-Fe-arsenate, new Tl-arsenates, fluorapatite, K-feldspar, muscovite, oxyphlogopite, Tl-pharmacosiderite, cinnabar, rutil
CD6-HS	Light-grey to light brownish	Gypsum, dolomite, calcite, quartz	Fangite, lorándite, orpiment	Ca-Mn-arsenate, fluorapatite, muscovite, rutil

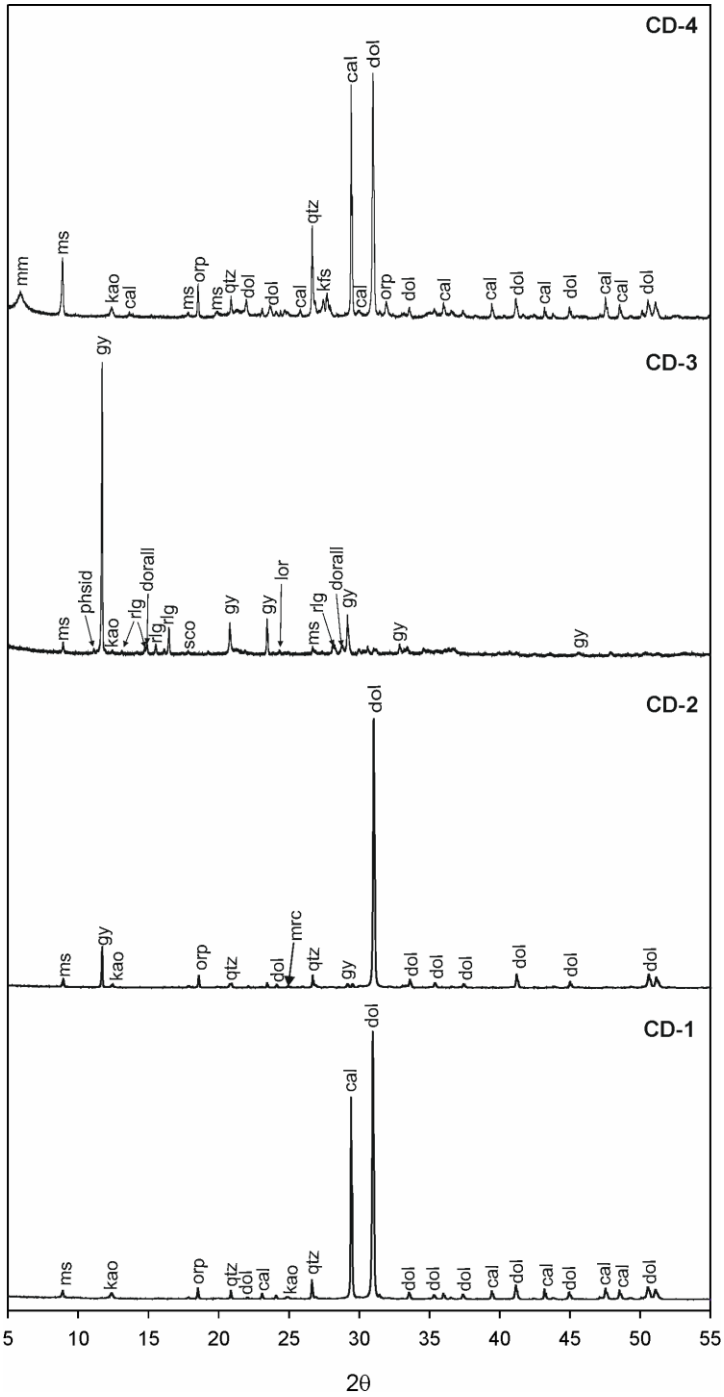

Figure 6: Diffractograms of the samples CD 1-4

Key: mm = montmorillonite; orp = orpiment; phsid = pharmacosiderite; dorall = dorallcharite; rlg = realgar; lor = lorándite; mrc = marcasite

Table 4: Overview of primary and secondary Tl minerals of Crven Dol

Mineral name	Chemical formula	Reference
Bernardite*	$TlAs_5S_8$	Pašava et al., 1989
Christite*	$TlHgAsS_3$	Makreski et al., 2014
Dorallcharite*	$TlFe_3^{+3}(SO_4)_2(OH)_6$	Balić-Žunić et al., 1993; this work
Fangite*	Tl_3AsS_4	El Goresy and Pavicevic, 1988; Frantz et al., 1994; this work
Jankovićite*	$Tl_5Sb_9(As,Sb)_4S_{22}$	Cvetković et al., 1995
Lorándite*	$TlAsS_2$	Balić-Žunić et al., 1995; this work
Parapierrotite*	$TlSb_5S_8$	John et al., 1995
Pictopaulite*	$TlFe_2S_3$	Balić-Žunić et al., 2008
Raguinite*	$TlFeS_2$	Laurent et al., 1969
Rebulite*	$Tl_5Sb_5As_8S_{22}$	Balić-Žunić et al., 2015
Simonite*	$TlHgAs_3S_6$	Engel et al., 1982
Thalliumpharmacosiderit*	$TlFe^{3+}{}_4(AsO_4)_3(OH)_4 \cdot 4H_2O$	Rumsey et al., 2014; Đorđević et al., 2021; this work
Vrbaite*	$Hg_3Tl_4As_8Sb_2S_{20}$	Boev et al., 2001
Avicennite	Tl_2O_3	This work
Tl-bearing Mn-oxides	3.1 to 3.8 at. % Tl	This work
NEW! Tl–M^{2+}–arsenates M^{2+}= Ca, Mg and/ or Mn	~ 3:1:1	This work
NEW! Tl–M^{2+}–arsenates	~ 2:1:1	This work
NEW! Tl–M^{2+}–arsenates	~ 1:1:1	This work
NEW! Tl–M^{2+}–arsenates	~ 1:3:2	This work

*Type locality

Table 5: Overview of primary and secondary As minerals of Crven Dol

Mineral name	Chemical formula	Reference
Arseniosiderite	$Ca_2Fe^{3+}_3(AsO_4)_3O_2 \cdot 3H_2O$	Đorđević et al., 2021; this work
Bernardite	$TlAs_5S_8$	Pašava et al., 1989
Christite	$TlHgAsS_3$	Makreski et al., 2014
Claudetite	As_2O_3	Boev et al., 2001
Fangite	Tl_3AsS_4	El Goresy and Pavicevic, 1988; Frantz et al., 1994; this work
Hörnesite	$Mg_3(AsO_4)_2 \cdot 8H_2O$	Rieck, 1993
Hydronium-pharmacosiderite	$(H_3O)Fe_4(AsO_4)_3(OH)_4 \cdot 4H_2O$	Đorđević et al., 2021; this work
Jankovićite	$Tl_5Sb_9(As,Sb)_4S_{22}$	Cvetković et al., 1995
Lorándite	$TlAsS_2$	Krenner, 1897; this work
Natropharmacosiderite	$Na_2Fe^{3+}_4(AsO_4)_3(OH)_5 \cdot 7H_2O$	Đorđević et al., 2021
Orpiment	As_2S_3	Percival and Radtke, 1994 and references therein; this work
Pharmacosiderite	$KFe^{3+}_4(AsO_4)_3(OH)_4 \cdot 6\text{-}7H_2O$	Đorđević et al., 2021; this work
Picropharmacolite	$Ca_4Mg(AsO_4)_2(HAsO_4)_2 \cdot 11H_2O$	Rieck, 1993
Realgar	As_4S_4	Rieck, 1993 and references threin; this work
Rebulite	$Tl_5Sb_5As_8S_{22}$	Balić-Žunić et al., 1982
Scorodite	$Fe^{3+}AsO_4 \cdot 2H_2O$	Percival, and Radtke, 1994; Đorđević et al., 2021, this work
Simonite	$TlHgAs_3S_6$	Engel et al., 1982
Talmessite	$Ca_2Mg(AsO_4)_2 \cdot 2H_2O$	Đorđević et al., 2021; this work
Thalliumpharmacosiderite	$TlFe^{3+}_4(AsO_4)_3(OH)_4 \cdot 4H_2O$	Rumsey et al., 2014; Đorđević et al., 2021; this work

Vrbaite*	$Hg_3Tl_4As_8Sb_2S_{20}$	Boev et al., 2001
NEW! Tl–M^{2+}–arsenates M^{2+}= Ca, Mg and/ or Mn	~ 3:1:1 (Mg- or Ca-dominant with Mg~Ca)	This work
NEW! Tl–M^{2+}–arsenates	~ 2:1:1 (mainly Mg- or Mn-dominant)	This work
NEW! Tl–M^{2+}–arsenates	~ 1:1:1 (Ca- or Mg-dominant, with major, but variable Fe)	This work
NEW! Tl–M^{2+}–arsenates	~ 1:3:2 (strongly Mn-dominant)	This work

Table 6: List of all minerals identified in Crven Dol within this study

Sulfides and sulfosalts		Phosphates	
Pyrite[1,2]	FeS_2	Flourapatite[1]	$Ca_5(PO_4)_3F$
Marcasite[1,2]	FeS_2	Arsenates	
Realgar[1]	As_4S_4	Arseniosiderite[1,2]	$Ca_2Fe^{3+}{}_3(AsO_4)_3O_2{\cdot}3H_2O$
Fangite[1]	Tl_3AsS_4	Talmessite[1,2]	$Ca_2Mg(AsO_4)_2{\cdot}2H_2O$
Orpiment[1,2]	As_2S_3	Tl-Pharmacosiderite[1]	$TlFe_4[(AsO_4)_3(OH)_4]{\cdot}4H_2O$
Cinnabar[1]	HgS	Scorodite[1,2]	$Fe^{3+}AsO_4{\cdot}2H_2O$
Lorándite[1,2]	$TlAsS_2$	new! Tl-M^{2+}-arsenates[1]	(M^{2+} = Mg, Mn, Fe, Ca) Tl:M:As ~ 3:1:1
Oxides		new! Tl-M^{2+}-arsenates[1]	(M^{2+} = Mg, Mn, Fe, Ca) Tl:M:As ~ 2:1:1
Rutile[1,2]	TiO_2	new! Tl-M^{2+}-arsenates[1]	(M^{2+} = Mg, Mn, Fe, Ca) Tl:M:As ~ 1:1:1 (Ca- or Mg-dominant, variable Fe content)
Quartz[1,2]	SiO_2	new! Tl-M^{2+}-arsenates[1]	(M^{2+} = Mg, Mn, Fe, Ca) Tl:M:As ~ 1:3:2 (strongly Mn-dominant)
Tl-bearing Mn-oxides[1]	3.1 to 3.8 at. % Tl		
Lepidocrocite[2]	γ-$Fe^{3+}O(OH)$	Silicates	
Avicennite[3]	Tl_2O_3	Flogopite[1]	$KMg_3(AlSi_3O_{10})(OH)_2$
Carbonates		K-feldspar[1]	$K(AlSi_3O_8)$
Siderite[2]	$FeCO_3$	Kaolinite[1]	$Al_2(Si_2O_5)(OH)_4$
Dolomite[1,2]	$CaMg(CO_3)_2$	Muscovite[1]	$KAl_2(AlSi_3O_{10})(OH)_2$
Calcit[1,2]	$CaCO_3$	Zircon[1,2]	$Zr(SiO_4)$
Sulfates		Montmorillonite[3]	$(Na,Ca)_{0.33}(Al,Mg)_2(Si_4O_{10})(OH)_2{\cdot}nH_2O$
Barite[1]	$BaSO_4$		
Dorallcharite[1]	$TlFe_3{}^{+3}(SO_4)_2(OH)_6$		
Gypsum[1,2]	$CaSO_4{\cdot}2H_2O$		
Hydroniumjarosite[1,3]	$(H_3O)Fe^{3+}{}_3(SO_4)_2(OH)_6$		

[1]SEM-EDS; [2]Raman; [3]PXRD

6.2.2 Primary minerals

PXRD analyzes of the sample CD-1 showed that besides dominant carbonate minerals (dolomite and calcite) and quartz, the main ore mineral is orpiment. According to the PXRD-measurement, in CD-2 and CD-4 orpiment is also the main primary phase. On the contrary, referring to the PXRD measurement, in CD-3, the most prominent primary sulfides are lorándite, $TlAsS_2$ and realgar, As_4S_4. The combination of SEM-EDX and Raman spectroscopy on the polished samples (CD-3A-HS, CD-4HS and CD-6HS) gave a more precise picture of the mineralogy of the waste dumps of Crven Dol. Except above mentioned lorándite, the major Tl-bearing primary phase was the mineral fangite, Tl_3AsS_4, found both in CD-4HS and CD-6HS, mostly crystallizing in the thin cracks of orpiment as tiny euhedral crystals up to 25 µm (Figure 7: Back-scattered electron images of sulfides
(b)). Fangite is also the primary source of thallium in the samples CD-1 and CD-4 (Đorđević et al., 2021), where it also crystallizes in the voids of orpiment. In the sample CD-3AHS, lorándite, (Figure 7: Back-scattered electron images of sulfides
(a)) is the primary Tl-source, similarly to the sample CD-3 (Đorđević et al., 2021). It appears in the form of prismatic, sometimes strongly weathered crystals up to ~525 µm in size and is often intergrown with realgar. Pyrite was found as the minor phase, mostly weathered, subhedral or anhedral and quite often framboidal (Figure 7: Back-scattered electron images of sulfides
(e)/(f)), mostly in the sample CD-3 and CD-3AHS. Small aggregates (around 5 µm) of arsenopyrite with 28 at.% As and 27 at.% of Tl were detected, intergrown with pyrite in siderite (CD-4HS). Also in CD-4HS tiny (~2 µm) crystals of cinnabar were detected. Shortened, it can be stated that the major primary minerals, and Fe and As sources in the investigated samples are pyrite and marcasite, realgar and orpiment, respectively. They are mostly quite altered, but occasionally appear as fresh grains/crystals.

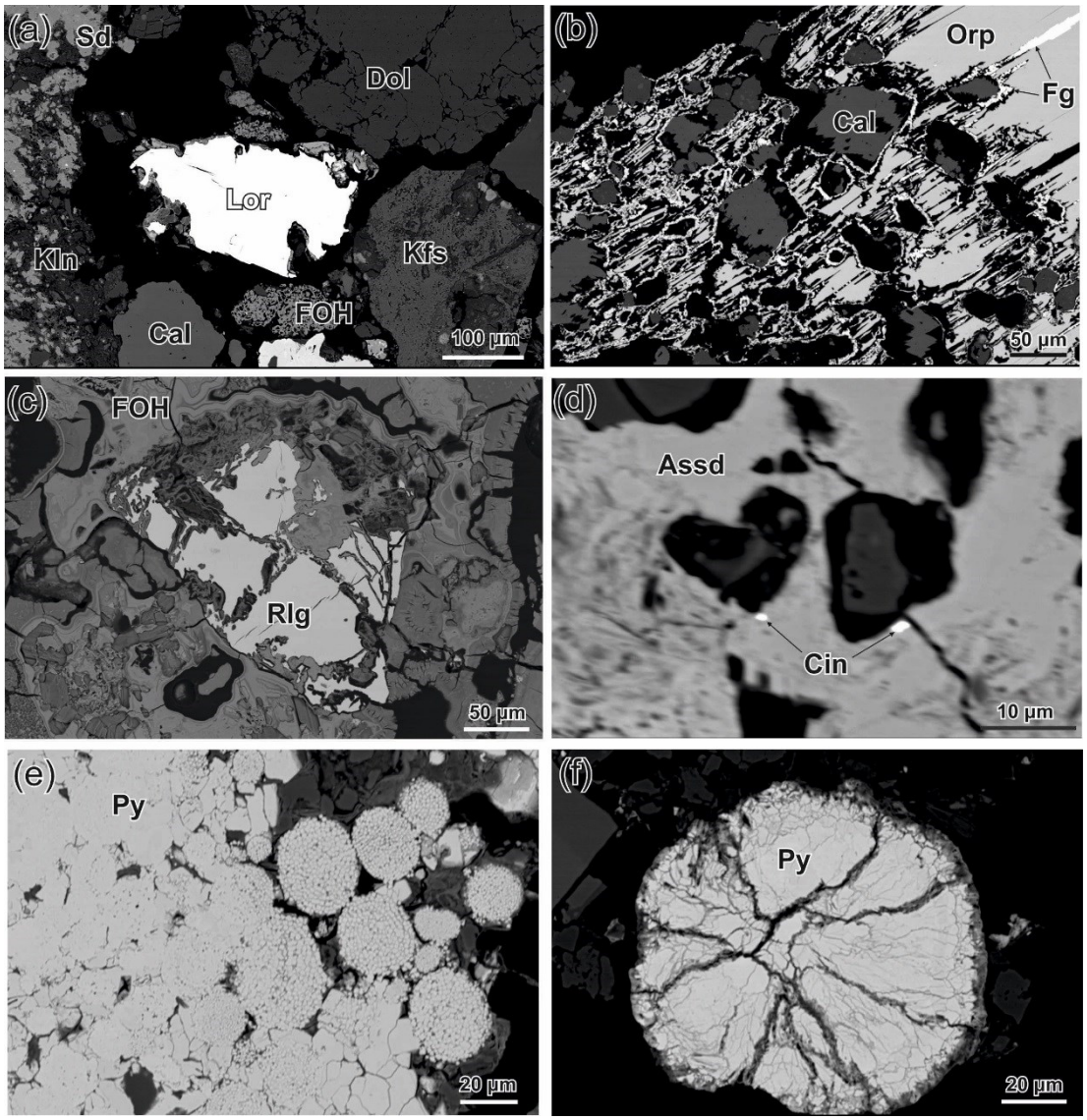

Figure 7: Back-scattered electron images of sulfides

(a) lorándite (Lor) with dolomite (Dol), kalifeldspar (Kfs), FOHs, calcite (Cal), kaolinite group (Kln) and siderite (Sd), (b) orpiment (Orp) next to calcite with a fangite (Fg)-fringe, (c) realgar (Rlg) with layered FOHs, (d) cinnabar (Cin) next to arseniosiderite (Assd), (e) pyrite (Py) with framboidal structure, (f) pyrite, strongly weathered

6.2.3 Secondary minerals

By using the combination of SEM-EDX and Raman spectroscopy on polished sections, a closer look at the secondary minerals were taken. The secondary mineralogy comprises mostly iron-oxyhydroxides (FOHs) especially amorphous iron-oxyhydroxides which occur as weathering products of Fe-sulfides (CD-3AHS), and various arsenates, mostly Ca-Fe-arsenates (CD-4HS and CD-6HS). Minor thalliumpharmacosiderite, $TlFe_4(AsO_4)_3(OH)_4 \cdot 4H_2O$, often along with traces of N (1.4 – 3.0 at. %) or P (0.1 – 0.2 at. %) was found in sample CD-3AHS mostly as tiny cubes and is often intergrown with dorallcharite and FOHs (Figure 9 (a) and 9(f)). N is either from leftover traces of dynamite, used while mining, or from decomposition from organic material. Thallium bearing scorodite (up to 1.7 at.%), $Fe^{3+}AsO_4 \cdot 2H_2O$ (CD-3AHS), as well as some new Tl-M(II)-arsenates (with M(II) being Ca, Mg and/or Mn) (CD-4HS and CD-6HS) were identified (Figure 14 (a) and (b)) and more particularly described in Chapter 6.3. Those new thallium arsenates were additionally analyzed with Raman spectroscopy. This resulted in quite broad bands appearing in two main spectral ranges, 350-600 and 700-900 cm^{-1} (Figure 11). Similarly to Tl-arsenates described by Đorđević et al. (2021) both spectral ranges are attributed to arsenate tetrahedra showing As–O symmetric bending and stretching modes for the two regions, respectively. Dissolved Tl while weathering was again reprecipitated as micaceous crystals of poorly crystalline Tl-M(II)-arsenates, Figure 11 and the Raman spectra with really broad bands of the arsenates spectra confirm that. These secondary thallium-metal arsenates (most of them are previously unknown mineral phases) occur in interstitial voids, around the margin of the other minerals (Figure 14 (c)) and (d)). Secondary thallium sulfate minerals were found as well. With dorallcharite (Figure 9 (d)) leading the way, as the Tl-analogue of jarosite. Initially found in Allchar, as its type locality, it occurs mostly associated with gypsum (Figure 9 (c)), thalliumpharmacosiderite $TlFe_4[(AsO_4)_3(OH)_4] \cdot 4H_2O$ (Figure 9 (a)) with thallium values between 2.1 and 4.6 at.% and amorphous Mn and Fe oxides and/ or arsenates. When Tl is removed from sulfide oxidation and afterwards preserved by the sulfate again, dorallcharite is formed. Considering that K^+ is being substituted by Tl^+ in jarosite, a broad solid-solution series occurs between dorallacharite and jarosite (Zhao and Gu, 2021). Tiny crystals (< 5 µm) of thallium bearing (2.2 at.%) hydroniumpharmacosiderite $(H_3O)Fe^{3+}{}_4(AsO_4)_3(OH)_4 \cdot 4H_2O$ were identified (Figure 9

(e)). Arseniosiderite, $Ca_2Fe^{3+}_3(AsO_4)_3O_2{\cdot}3H_2O$ (Figure 12) appears to be the most common phase among the arsenates with mostly fine-grained aggregates (Figure 10 (a) and (d), also Figure 8(d)) and often intergrown with dolomite and talmessite $Ca_2Mg(AsO_4)_2{\cdot}2H_2O$ (Figure 8 (f)). Accordingly, well-crystalline aggregates of talmessite were found intergrown with dolomite and minor arseniosiderite (Figure 10(c)) as well as inside some fissures of arseniosiderite aggregates (Figure 10(c) and (d)) and Figure 12.

This could also be proven with Raman spectroscopy (Figure 12). The rather fine band of arseniosiderite in the Raman spectra (Figure 12) proofs again the crystalline character of this phase, also its Raman spectra (391, 858 and 931 cm^{-1}) compare almost identically to those Raman spectra of arseniosiderite from the Smolotely-Líšnice (Drahota et al., 2018), where they measured Raman bands at 392, 859 and 936 cm^{-1}. In AsO_4 stretching vibrations for talmessite were observed at 785, 836 and 875 cm^{-1}. This Raman bands compare quite well with the Raman bands reported for natural talmessite by Frost (2009). The chemical composition of the five investigated Ca-Fe-arsenate aggregates (sample CD-4) were measured with stoichiometric mean concentrations of (in at.%): O = 66.4, Fe = 14.2, As = 11.3, Ca = 6.8, S = 0.3, P = 0.3, Si = 0.4, Tl = 0.1, Mg = 0.3, Mn = 0.2, Sr = 0.1. These values compare well with the mean values for the arseniosiderites from Allchar deposit published by Đorđević et al. (2021). Around weathered calcite, Ca-Mn-arsenate was detected (Figure 10(b)). Five aggregates were measured with a mean concentration of (in at. %): O = 67.0, Al = 0.7, Si = 1.0, S = 0.3, K = 0.2, Ca = 8.8, Mn = 10.1, Fe = 0.8, As = 22.4, and Tl = 0.1. PXRD of the hand specimens (CD3A-HS and CD3A2-HS, Figure 8) showed the visible presence of hydroniumjarosite, $(H_3O)Fe^{3+}_3(SO_4)_2(OH)_6$ (Figure 9(b)) and rare Tl(III) mineral avicennite, Tl_2O_3 (Figure 8). That is the very first time this mineral was identified in Allchar deposit.

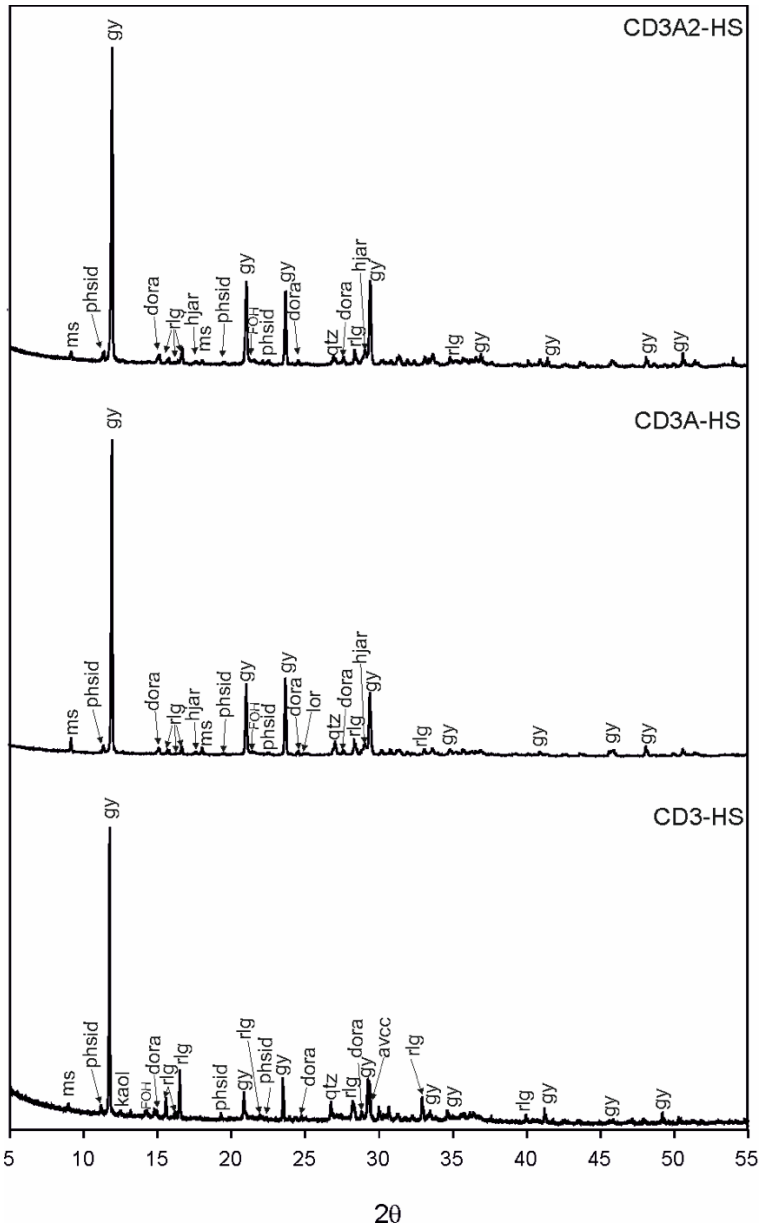

Figure 8: Diffractograms of the hand specimens

Key: phisd. = pharmacosiderite; dora = dorallcharite; rlg = realgar; avcc = avicennite; hjar = hydroniumjarosite

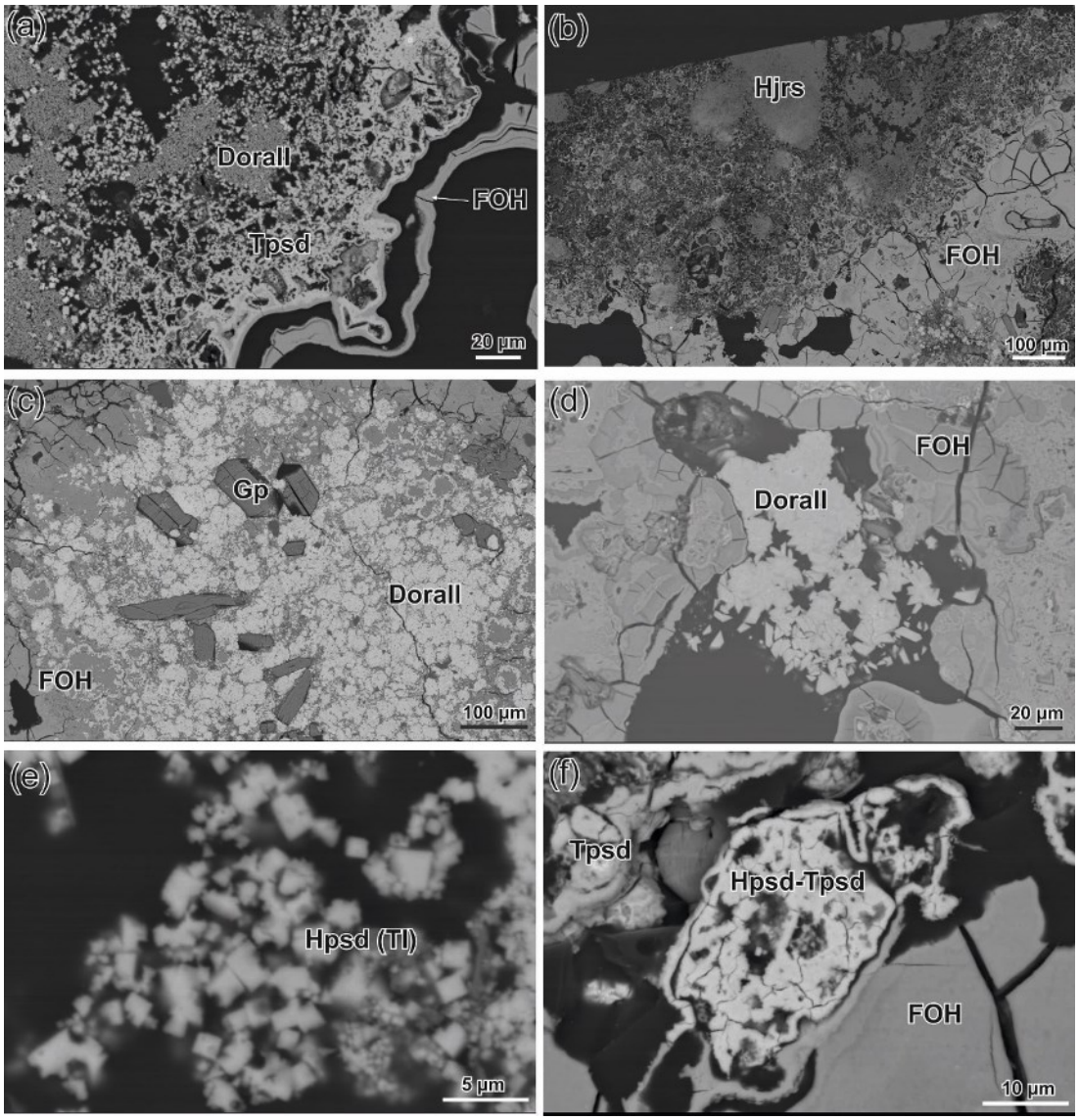

Figure 9: Back scattered images of sulfides

(a) thalliumpharmacosiderite (Tpsd) intergrown with dorallcharite (Dorall) and FOHs, (b) hydroniumjarosite (Hjrs) with FOHs, (c) gypsum (Gp) crystalls in dorallcharite with FOHs, (d) dorallcharite crystalls with FOH

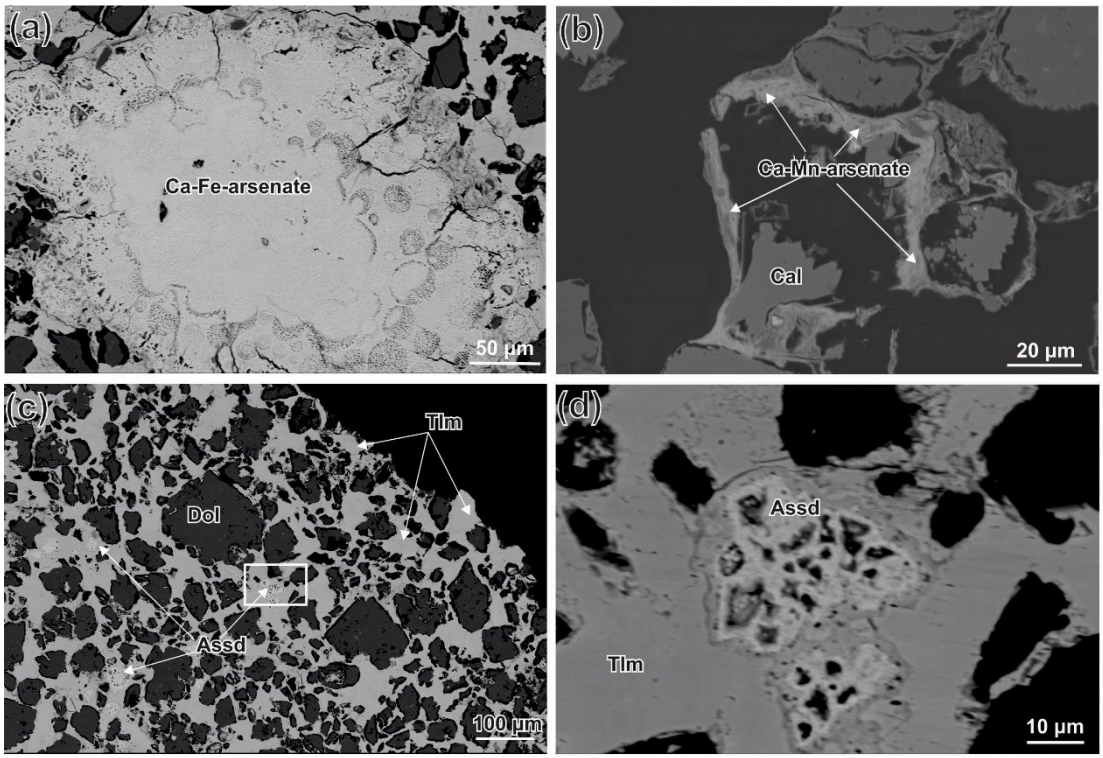

Figure 10: Back scattered electron images of the secondary Tl and As minerals

(a) globular aggregates of arseniosiderite (Assd), (b) Ca-Mn arsenate around weathered calcite (Cal), (c) talmessite (Tlm) intergrown with dolomite (Dol) and minor arseniosiderite, (d) finely grained arseniosiderite in talmessite

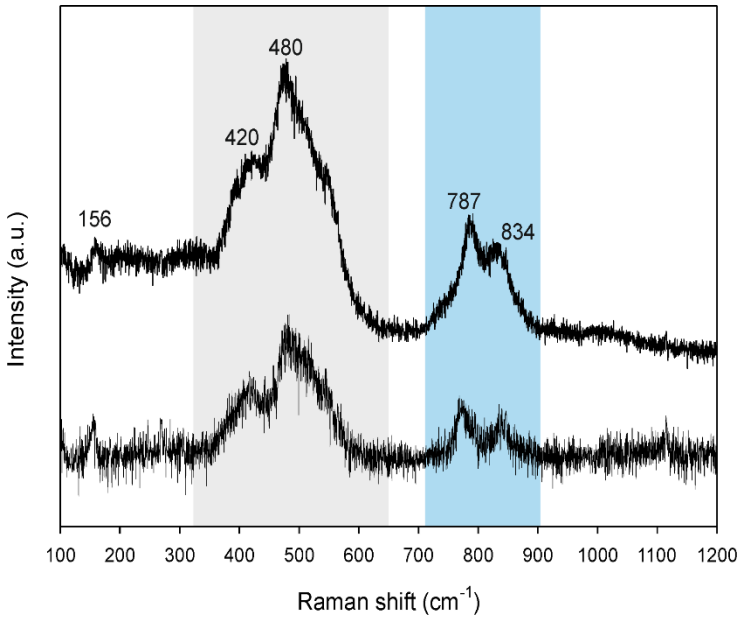

Figure 11: Raman spectra of newly found Tl-M(II)-arsenates

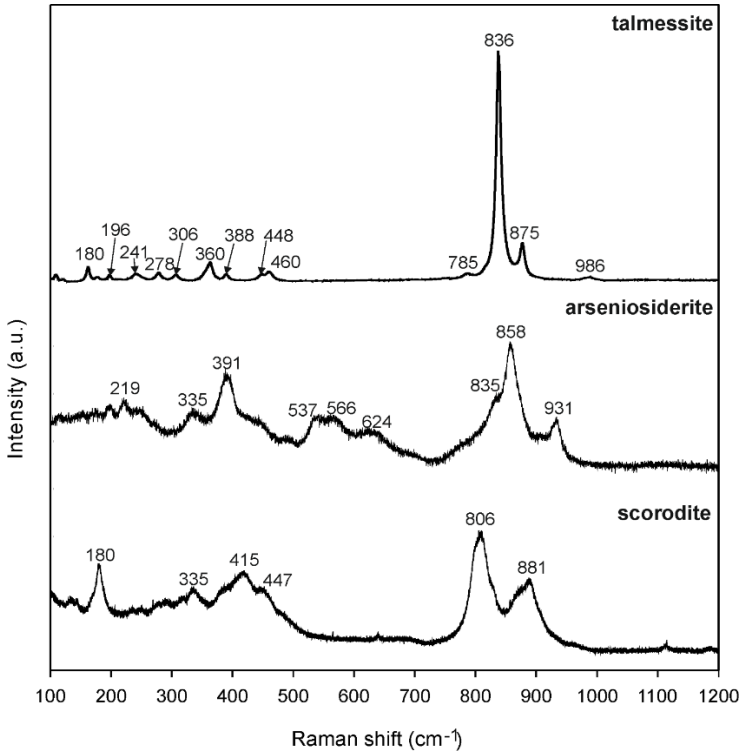

Figure 12: Raman spectra of common secondary arsenates

6.3 New findings

The existence of small (up to 100 µm) aggregates of at least five previously unknown secondary thallium phases at the present stage of this study were proved:

1) **Tl–M^{2+}–arsenates** (Figure 13) with approximate Tl:M:As ratios of

(i) ~ 3:1:1 (Mg- or Ca-dominant with Mg~Ca);

(ii) ~ 2:1:1 (mainly Mg- or Mn-dominant);

(iii) ~ 1:1:1 (mainly Ca- or Mg-dominant, with major, but variable Fe);

(iv) ~ 1:3:2 (strongly Mn-dominant, with apparent Si content).

All these arsenates show slightly to distinctly variable ratios of the M^{2+} cations (Ca, Mg and/ or Mn) within individual aggregates.

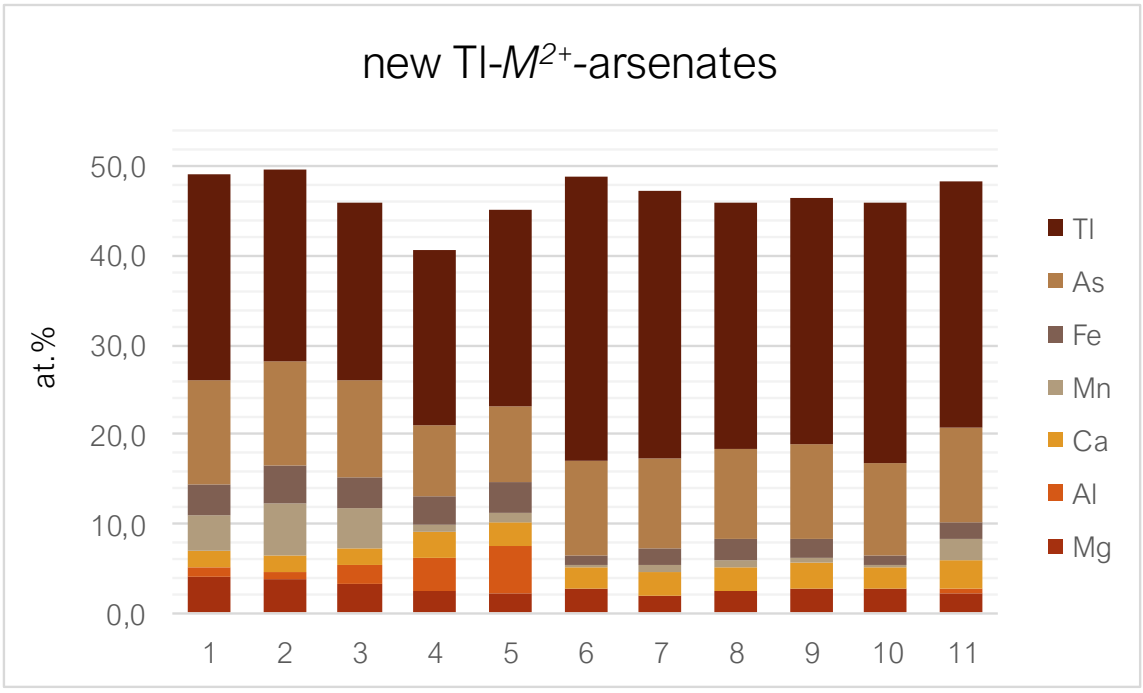

Figure 13: Chemistry of the new Tl–M(II)–arsenates

2) **Cryptomelane-type Tl-bearing Mn oxides** (Figure 14 (b); Table 7) with (3.1 to 3.8 at. % Tl), probably closely related to newly described mineral thalliomelane, $Tl(Mn^{4+}_{7.5}Cu^{2+}_{0.5})O_{16}$ (Gołębiowska et al., 2021).

SEM-EDX values of the Mn-oxides associated with Ca (3.5 to 3.9 %) and Tl (3.1 to 3.8 %) are given in Table 7. Figure 14(b) shows that these Mn-oxides were intergrown as a weathering crust to newly found Tl-metal-arsenates. Table 7 shows the SEM-EDX values for three measure points of this new, cryptomelane-type Tl-bearing Mn oxides.

Table 7: SEM-EDX values (in at.%) of Mn-oxides (CD-4HS)

O	Mg	Al	Si	S	Ca	Mn	Fe	As	Ba	Tl
60	0.5	0.3	0.0	0.8	3.9	28.7	0.8	1.0	0.0	3.8
61	0.5	0.0	0.2	0.8	3.5	28.8	1.0	0.7	0.1	3.6
64	0.6	0.5	0.7	0.0	3.5	25.6	1.1	0.7	0.0	3.1

3) **Avicennite**, Tl_2O_3 (Figure 8) was detected using PXRD in the sample CD3-HS. This is the first time, this mineral was found in Allchar deposit. Avicennite is one of four known natural minerals of Tl(III) (next to amgaite, chrysothallite and kalithallite). Avicennite is typically associated with manganese oxides and the occurrence of one of these Tl(III) minerals imply that there may be other mechanisms accountable for the oxidation of Tl(I) to Tl(III) (Zhao and Gu, 2021).

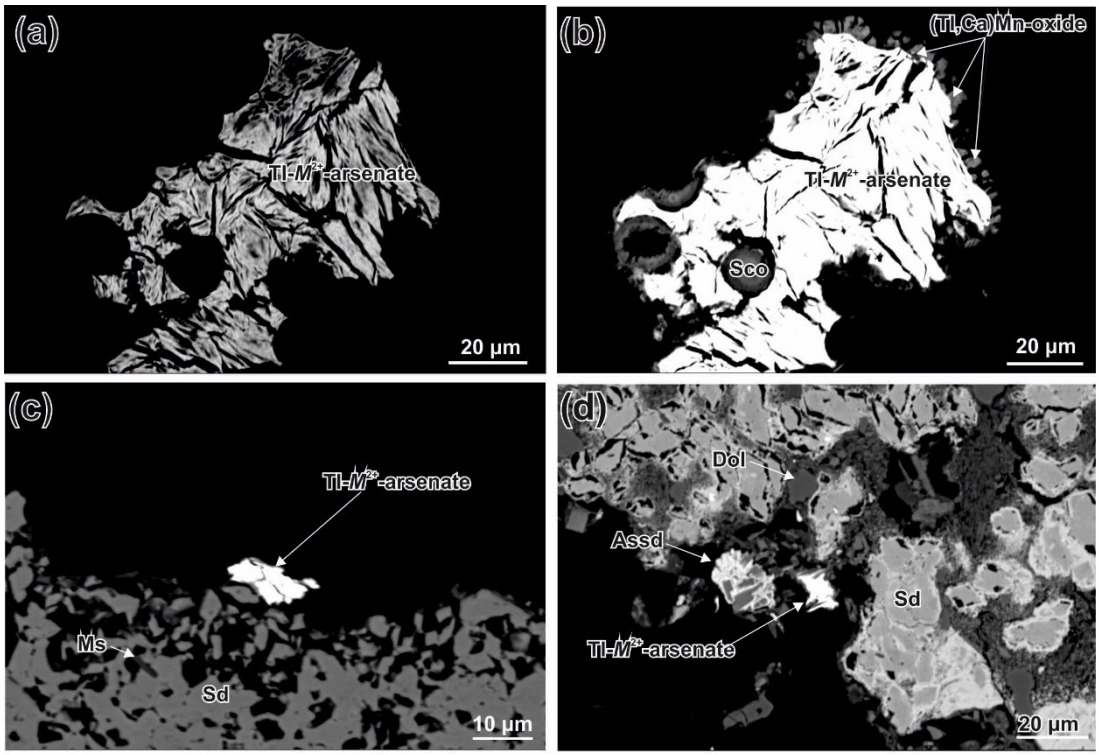

Figure 14: Backscattered electron images of Tl–M(II)–arsenates

(a) Tl-M(II)-arsenates (M^{2+} = Mg, Ca, Mn, Fe) (very high contrast), (b) Tl-M(II)-arsenates intergrown with globular scorodite (sco) and Tl-Mn-oxide , (c) Tl-M(II)-arsenate with siderite (sd) and minor muscovite (ms), (d) Tl-M(II)-arsenate aggregate in a mixture of sd, dol and arsd

7 Discussion

7.1 Thallium and arsenic retention by secondary minerals

By the weathering of thallium, arsenic, antimony and iron sulfides and sulfosalts, secondary minerals form. The nature of these secondary arsenic and thallium phases are most importantly induced by the kind of primary mineralization which took place and whether or not carbonate minerals are present for pH-buffering. These sulfides will weather under naturally, oxidizing conditions, which leads to a relocation of the major elements As, Tl, S and Fe. Fe mainly enters Ca-Fe arsenates and FOHs, in the carbonate rich samples (Table 1 and Figure 4). Sb is mostly incorporated into pyrite and was also found in traces in orpiment (0.6 at. %), measured by SEM-EDX. Resolved arsenic is implemented in many crystalline arsenates like talmessite or arseniosiderite. Thallium is mostly integrated in previously unknown Tl-M(II)-arsenates, which are quite abundant, with thallium values between 27.6 and 31.8 at. %, according to SEM-EDX measurements. These arsenates are not really crystalline and appear chemically heterogeneous with Tl:As ratios of approximately 3:1, 2:1, 1:1 and 1:2. With M^{2+} being Ca and Mg and or Mn, they do not match with any arsenate known before. Using SEM-EDX, it was observed that thallium also has a strong affinity for manganese oxides (Figure 14 (b)) where a Tl and Ca bearing Mn-oxide-crust, with Tl values from 3.1 to 3.8 at. % (Table 7) remodels as a weathering crust along newly discovered Tl-M(II)-arsenates. This Tl and Ca bearing Mn-oxidecould also be a new mineral phase and belongs most likely to the cryptomelane group. The preference of Tl to incorporate into secondary Mn-oxides, rather than into FOHs can be explained by the simple insertion of thallium cations into the tunnely vacancy of the crystal structures of most Mn-oxide minerals, particularly into the cryptomelane group (Aguilar-Carillo et al., 2020; Gołębiowska et al., 2021). This affinity could lead to an oxidation from Tl(I) to Tl(III) through sorbing of birnessites or a cryptomelane-type Tl-bearing Mn oxides. It is possible that avicennite, which was found in CD-3-HS using PXRD, was formed this way. The other possibility is by strongly altering of carlinite. Both minerals, carlinite and birnessite nevertheless were not clearly verifiable

throughout this study. Those manganese oxides however seem to be a further thallium source in soils of this area, based on laboratory sorption as well as on spectroscopic studies from Voegelin et al., 2015 and Wick et al., 2018 about those phases. The richness of carbonate rocks in sample CD-3 indicates that dissolved iron was mostly incorporated into dorallcharite, scorodite, abundant FOHs and also rare pharmacosiderite-supergroup minerals (Table 9). This secondary mineralogy implies partial acidification in some micro-environments of Crven Dol samples (CD-3). This originates from the fact of frequent Fe-sulfides weathering. Figure 7 (e) and (f) shows strongly weathered pyrites. As dorallcharite only forms under intensely acidic conditions, it is proven that there are at least temporary and locally acidic conditions (Đorđević et al., 2021). Another typical weathering product of acidic environments are clay minerals of the kaolinite-group. Those clay minerals are containing small amounts of Tl and appear tabular. Tl-bearing hydroniumjarosite was detected with pseudo-cubic crystals between 0.6-0.8 µm. Dorallcharite as a prime mineral of this study and a member of the alunite group (Figure 8), shows the possibility to act as a sink for potentially toxic elements such as Tl. It also incorporates iron, which is otherwise mostly absorbed by Ca-Fe-arsenates and FOHs.

Table 8: Members of alunite group minerals

Mineral name	Chemical formula	Reference
Ammonioalunite	$(NH_4)Al_3(SO_4)_2(OH)_6$	Bayliss et al., 2010
Argentojarosite	$AgFe^{3+}{}_3(SO_4)_2(OH)_6$	Hendricks, 1937
Beaverite-(Cu)	$Pb(Fe^{3+}{}_2Cu)(SO_4)_2(OH)_6$	Bayliss et al., 2010
Beaverite-(Zn)	$Pb(Fe^{3+}{}_2Zn)(SO_4)_2(OH)_6$	Bayliss et al., 2010
Dorallcharite	$TlFe^{3+}{}_3(SO_4)_2(OH)_6$	Balić-Žunić et al., 1994
Hydroniumjarosite	$(H_3O)Fe^{3+}{}_3(SO_4)_2(OH)_6$	Đorđević et al., 2021
Jarosite	$KFe^{3+}{}_3(SO_4)_2(OH)_6$	Đorđević et al., 2021
Natrojarosite	$NaFe_3(SO_4)_2(OH)_6$	Grey et al., 2011
Plumbojarosite	$Pb_{0.5}Fe^{3+}{}_3(SO_4)_2(OH)_6$	Bayliss et al., 2010

Arseniosiderite and mostly talmessite act as the sinks for dissolved arsenic, but in sample CD3A-HS especially, arsenic is also incorporated into the pharmacosiderite supergroup minerals (.

Table 9). In this group, the minerals are not only incorporating arsenic but also thallium. Using SEM-EDX following Tl-values have been confirmed: 3.1-4.6 at. % Tl for thalliumphramcosiderite and up to 2.2 at. % of Tl for hydronium-pharmacosiderite.

Table 9: Pharmacosiderite supergroup minerals

Mineral name	Chemical formula	Reference
Pharmacosiderite group		
Bariopharmacosiderite-C	$Ba_{0.5}Fe^{3+}_4(AsO_4)_3(OH)_4 \cdot 2.52H_2O$	Hager et al., 2010
Bariopharmacosiderite-Q	$Ba_{0.5}Fe^{3+}_4(AsO_4)_3(OH)_4 \cdot 6.16H_2O$	Peacor and Dunn, 1985
Caesiumpharmacosiderite	$CsFe_4[(AsO_4)_3(OH)_4] \cdot 4H_2O$	Mills et al., 2013
Hydroniumpharmacosiderite	$(H_3O)Fe_4(AsO_4)_3(OH)_4 \cdot 4H_2O$	Đorđević et al., 2021; this work
Natropharmacosiderite	$KFe^{3+}_4(AsO_4)_3(OH)_4 \cdot 6\text{-}7H_2O$	(Majzlan et al., 2019)
Plumbopharmacosiderite	$Pb_{0.5}Fe^{3+}_4(AsO_4)_3(OH)_4 \cdot 5H_2O$	Vignola et al., 2018
Strontiopharmacosiderite	$Sr_{0.5}Fe_4[(AsO_4)_3(OH)_4] \cdot 4H_2O$	Mills et al., 2014
Thalliumpharmacosiderite	$TlFe_4[(AsO_4)_3(OH)_4] \cdot 4H_2O$	Rumsey et al., 2014
Pharmacoalumite group		
Bariopharmacoalumite	$Ba_{0.5}Al_4(AsO_4)_3(OH)_4 \cdot 4H_2O$	Mills et al., 2011
Hydroniumpharmacoalumite	$(H_3O)Al_4(AsO_4)_3(OH)_4 \cdot 4.5H_2O$	Hochleitner et al., 2013
Natropharmacoalumite	$NaAl_4(AsO_4)_3(OH)_4 \cdot 4H_2O$	Rumsey et al., 2010
Pharmacoalumite	$KAl_4(AsO_4)_3(OH)_4 \cdot 6.5H_2O$	Rumsey et al., 2010
Ivanyukite group		
Ivanyukite-Cu	$CuTi_4(SiO_4)_3(OH)_2O_2 \cdot 7H_2O$	Yakovenchuk et al., 2009
Ivanyukite-K	$K_2Ti_4(SiO_4)_3(OH)_2O_2 \cdot 9H_2O$	Yakovenchuk et al., 2009
Ivanyukite-Na	$Na_2Ti_4(SiO_4)_3(OH)_2O_2 \cdot 6H_2O$	Yakovenchuk et al., 2009
Ivanyukite-Na-C	$Na_2Ti_4(SiO_4)_3(OH)_2O_2 \cdot 6H_2O$	Yakovenchuk et al., 2009

8 Conclusion

There is a lack of sufficient investigations on secondary Tl and As secondary minerals and their behaviour as reservoirs for the toxic elements. The understanding of the mobilization of those secondary minerals and their function to uptake toxic elements and in addition to it, in general, Tl speciation is the primary goal of this study.

New thallium and arsenic reservoirs in mine waste and technosol samples of the Crven Dol locality, an extremely Tl-rich area in North Macedonia, were newly identified within this study. Due to a well-developed secondary Tl-mineralogy, the Tl speciation differs here from that observed elsewhere. It was possible to detect up to five new thallium secondary phases. While secondary Tl-bearing minerals are lacking in soil horizons, the Tl(I) adsorption onto micaceous phyllosilicates (mainly illite) plus Tl(I) and Tl(III) adsorption onto Tl-/ Ca- bearing Mn-oxides has been known as the dominant thallium retention mechanism, before (Wick et al., 2020). Nevertheless, in a Tl-extreme environment, like Crven Dol, Allchar deposit, when illite and Mn-oxides are either missing and/ or depleted, Tl minerals are formed and store thallium. These Tl-minerals are mainly arsenates or sulfates. Those results show the demand for more investigations on Tl speciation in Tl-rich environments. In addition, avicennite Tl_2O_3, a Tl(III) mineral, could be confirmed for the first time in the Allchar deposit. Fortunately because of the all in all great carbonate-buffering along the deposit, it stands to reason that this neutral pH slows down the alteration progress of the sulfides, so that the risk of acid mine drainage is vanishingly low. Nonetheless, the contamination with arsenic and thallium in the soil stays abundant, as it is not depending on the AMD. As the Allchar locality is quite remote, there is not much of a study or investigation on the interdependency between the oxidation zone of this naturally Tl- and As deposit and the surrounding ecosystem. Either way, the treatment of the extremely Tl- and As- polluted soils depends highly on the character of the Tl- and As- bearing phases. This means, a full characterization of thallium and arsenic retention through secondary minerals is necessary to understand their movements and for a successful remediation plan for contaminated soils.

References

Aguilar-Carrillo, J., Herrera-García, L., Reyes-Domínguez, I.A., Gutiérrez, E.J. (2020): Thallium (I) sequestration by jarosite and birnessite: Structural incorporation vs surface adsorption. Environmental Pollution, 257, 13492–113503.

Alderton, D.; Serafimovski, T.; Burns, L.; Tasev, G. (2014): Distribution and mobility of arsenic and antimony at mine sites in FYR Macedonia. Carpathian Journal of Earth and Environmental Sciences, 9, 43–56.

Allmann, R.; Kern, A. (2013): Röntgen-Pulverdiffraktometrie: Rechnergestützte Auswertung, Phasenanalyse und Strukturbestimmung (Vol. 29). Springer-Verlag.

Amthauer, G.; Pavićević, M. K.; Jelenković, R.; El Goresy, A.; Boev, B.; Lazić, P. (2012): State of geoscientific research within the lorándite experiment (LOREX): Mineralogy and Petrology, 105, 157–169.

ATSDR (2019): ATSDR Annual Report 2019. Available online at

https://www.atsdr.cdc.gov/2019atsdrannualreport/index.html, updated on 7/3/2022, checked on 7/3/2022.

Bačeva, K.; Stafilov, T.; Šajn, R.; Tănăselia, C.; Makreski, P. (2014): Distribution of chemical elements in soils and stream sediments in the area of abandoned Sb-As-Tl Allchar mine, Republic of Macedonia. Environmental Research, 133, 77–89.

Balić Žunić, T., Stafilov, T. & Tibljaš, D. (1993): Distribution of thallium and the ore genesis at the Crven Dol locality in Alšar. Geologica Macedonica, 7, 45-52.

Balić-Žunić, T.; Karanović, L.; Poleti, D. (2008): Crystal Structure of Picotpaulite, $TlFe_2S_3$, from Allchar, FYR Macedonia. Acta Chimica Slovenica, 55, 801-809.

Balić-Žunić, T.; Šćavničar, S.; Engel, P. (1982): The crystal structure of rebulite, $Tl_5Sb_5As_8S_{22}$. Zeitschrift für Kristallographie - Crystalline Materials, 160, 109–125.

Balic-Žunić, T.; Moëlo, Y.; Karanović, L.; Berlepsch, P. (2015): The solid solutions of rebulite and jankovićite in the phase system Tl_2S-As_2S_3-Sb_2S_3. Macedonian Journal of Chemistry and Chemical Engineering, 34, 125–132.

Balic-Žunić, T.; Moëlo, Y.; Lončar, Z.; Micheelsen, H. (1994): Dorallcharite, $Tl_{0.8}K_{0.2}Fe_3(SO_4)_2(OH)_6$, a new member of the jarosite-alunite family. European Journal of Mineralogy, 6, 255–263.

Balić-Žunić, T.; Stafilov, T.; Tibljaš, D. (1993): Distribution of thallium and the ore genesis at the Crven Dol locality in Alšar. Geologica Macedonica, 7, 45–52.

Bayliss, P.; Kolitsch, U.; Nickel, E. H.; Pring, A. (2010): Alunite supergroup: recommended nomenclature: Mineralogical magazine, 74, 919–927.

Boev, B.; Bermanec, V.; Serafimovski, T.; Lepitkova, S.; Mikulcic, S.; Soufek, M.; Jovanovski, G.; Stafilov, T.; Najdoski, M (2001): Allchar mineral assemblage. Geologica Macedonica, 15, 1–23.

Boev, B.; Jelenković, R. (2012): Allchar deposit in Republic of Macedonia—petrology and age determination. Petrology—New perspectives and applications, InTech, 131-168.

Boev, I.; Boev, B. (2015): The Crven Dol Arsenic-Thalium Mineralization in Alsar Depost in the Republic of Macedonia. Natural Resources and Technology, 9, 59-76.

Bowell, R.; Alpers, C.; Jamieson, H.; Nordstrom, K.; Majzlan, J. (2014): The environmental geochemistry of arsenic an overview. Reviews in Mineralogy and Geochemistry, 79, 1--16.

Chen, M.; Wu, P.; Li, S.; Yang, S.; Lin, Z.; Dang, Z. (2019): The effects of interaction between vermiculite and manganese dioxide on the environmental geochemical process of thallium. Science of The Total Environment, 669, 903–910.

Courtin-Nomade, A.; Rakotoarisoa, O.; Bril, H.; Grybos, M.; Forestier, L.; Foucher, F.; Kunz, M. (2012): Weathering of Sb-rich mining and smelting residues: Insight in solid speciation and soil bacteria toxicity.Geochemistry, 72, 29–39.

Craw, D.; Bowell, R. J. (2014): The characterization of arsenic in mine waste. Reviews in Mineralogy and Geochemistry, 79, 473–505.

Cvetković, Lj.; Boronikhin, V. A.; Pavićević, M. K.; Krajnović, D.; Gržetić, I.; Libowitzky, E.; Giester, G.; Tillmanns, E. (1995): Jankovićite, $Tl_5Sb_9(As,Sb)_4S_{22}$, a new Tl-sulfosalt from Allchar, Macedonia: Mineralogy and Petrology, 53, 125–131.

D'Orazio, M.; Biagioni, C.; Dini, A.; Vezzoni, S. (2017): Thallium-rich pyrite ores from the Apuan Alps, Tuscany, Italy: constraints for their origin and environmental concerns. Mineralium Deposita, 52, 687–707.

Đorđević, T.; Drahota, P.; Kolitsch, U.; Majzlan, J.; Peřestá, M.; Kiefer, S. et al. (2021): Synergetic Tl and As retention in secondary minerals: An example of extreme arsenic and thallium pollution. Applied Geochemistry, 135, 105–114.

Đorđević, T.; Kolitsch, U.; Drahota, P.; Peřestá, M.; Majzlan, J.; Kiefer, S.; Tasev, G., Serafimovski, T.; Boev, I.; Boev, B. (2020): Mobility of Tl and Hg in the As-rich waste dumps of adit no. 25, former Allchar.

Drahota, P.; Filippi, M. (2009): Secondary arsenic minerals in the environment: a review. Environment International, 35, 1243–1255.

Drahota, P., Kulakowski, O., Culka, A., Knappová, M., Rohovec, J., Veselovský, F., Racek,M. (2018): Arsenic mineralogy of near-neutral soils and mining waste at the Smolotely-Líšnice historical gold district, Czech Republic. Applied Geochemistry, 89, 243–254.

El Goresy, A.; Pavicevic, M. K. (1988): A new thallium mineral in the Alshar deposit in Yugoslavia. Naturwissenschaften, 75, 37–39.

Engel, P.; Nowacki, W.; Balić-Žunić, T.; Šćavnićar, S. (1982): The crystal structure of simonite, $TlHgAs_3S_6$. Zeitschrift für Kristallographie - Crystalline Materials, 161, 159–166.

Frantz, E.; Palme, H.; Todt, W.; Goresy, A. E.; Pavicevic, M. (1994): Geochemistry of Tl-As minerals and host rocks at Allchar (FYR Macedonia). Neues Jahrbuch für Mineralogie-Abhandlungen, 167, 359–400.

Frost, R.L. (2009): Raman and infrared spectroscopy of arsenates of the roselite and fairfieldite mineral subgroups. Spectrochimica Acta, A71, 1788–1794.

Ginibre, C.; Wörner, G.; Kronz, A. (2004): Structure and Dynamics of the Laacher See Magma Chamber (Eifel, Germany) from Major and Trace Element Zoning in Sanidine: a Cathodoluminescence and Electron Microprobe Study. Journal of Petrology, 45, 2197–2223.

Grey, I.E.; Scarlett, N.V.Y.; Bordet, P.; Brand, H.E.A. (2011): Jarosite–butlerite intergrowths in non-stoichiometric jarosites: crystal chemistry of monoclinic natrojarosite–hydroniumjarosite phases. Mineralogical Magazine, 75: 2775--2791.

Goldstein, J. I.; Newbury, D. E.; Echlin, P.; Joy, D. C.; Lyman, C. E.; Lifshin, E. Sawyer, L.; Michael, J.R. (2003): Scanning Electron Microscopy and X-ray Microanalysis. Third Edition. Boston, MA: Springer.

Gołębiowska, B.; Pieczka, A.; Zubko, M.; Voegelin, A.; Göttlicher, J.; Rzepa, G. (2021): Thalliomelane, $TlMn_{7.5}^{4+}Cu_{0.5}^{2+}O_{16}$, a new member of the coronadite group from the preglacial oxidation zone at Zalas, southern Poland. American Mineralogist, 109, 2020–2027.

Hager, S. L.; Leverett, P.; Williams, P. A.; Mills, S. J.; Hibbs, D. E.; Raudsepp, M.; Kampf, A.R.; Birch, W.D. (2010): The single-crystal X-ray structures of bariopharmacosiderite-C, bariopharmacosiderite-Q and natropharmacosiderite. The Canadian Mineralogist, 48, 1477–1485.

Hendricks, S. B. (1937): The crystal structure of alunite and the jarosites. American Mineralogist, 22, 773–784.

Herath, I.; Vithanage, M.; Bundschuh, J.; Maity, J. P.; Bhattacharya, P. (2016): Natural arsenic in global groundwaters: distribution and geochemical triggers for mobilization: In Current Pollution Reports 2, 68–89.

Herrmann, J.; Voegelin, A.; Palatinus, L., Mangold, S.; Majzlan, J. (2018): Secondary Fe–As–Tl mineralization in soils near Buus in the Swiss Jura Mountains. European Journal of Mineralogy, 30, 887–898.

Hochleitner, R.; Fehr, K.T.; Kaliwoda, M.; Günther, A.; Schmahl, W.W. and Park, S. (2013): Hydroniumpharmacoalumite, IMA 2012-050. CNMNC Newsletter No. 16, August 2013, page 2699; Mineralogical Magazine, 77, 2695–2709.

Hofmann, B. A.; Knill, M. D. (1996): Geochemistry and genesis of the Lengenbach Pb-Zn-As-Tl-Ba-mineralisation, Binn Valley, Switzerland. Mineralium Deposita, 31, 319–339.

Janković, S.; Jelenković, R. (1994): Thallium mineralization in the Allchar Sb-As-Tl-Au deposit. Neues Jahrbuch fur Mineralogie-Abhandlungen, 167, 283–298.

Jezek, B. (1912): Vrbait, ein neues Thallium Mineral von Allchar in Macedonian. Zeitschrift für. Kristallographie, 51, 365–378.

John, Z.; Picot, P.; Hak, J.; Kvaček, M. (1975): La parapierrotite, un nouveau minéral thallifère d'Allchar (Yougoslavie). Tschermaks Mineralogische und Petrographische Mitteilungen, 22, 200–210 (in French).

Kasatkin, A.V.; Plášil, J.; Makovicky, E.; Chukanov, N.V.; Škoda, R.; Agakhanov, A.A.; Tsyganko, M.V. (2022): Gungerite, $TlAs_5Sb_4S_{13}$, a new thallium sulfosalt with a complex structure containing covalent As-As bonds. American Mineralogist, 107, 1164–1173.

Krenner, J.A. (1897): Lorándit, ein neues Thallium-mineral von Allchar in Macedonien. Zeitschrift für Kristallographie und Mineralogie, 27, 98–99.

Kyono, A. (2005): Light-induced degradation dynamics in realgar: in situ structural investigation using single-crystal X-ray diffraction study and X-ray photoelectron spectroscopy. American Mineralogist, 90, 1563–1570.

Kyono, A.; Kimata, M. (2004): Structural variations induced by difference of the inert pair effect in the stibnite-bismuthinite solid solution series $(Sb,Bi)_2S_3$. American Mineralogist, 89, 932–940.

Larios, R.; Fernández-Martínez, R.; Álvarez, R.; Rucandio, I. (2012): Arsenic pollution and fractionation in sediments and mine waste samples from different mine sites. The Science of the total environment, 431, 426–435.

Laurent, Y.; Picot, P.; Pierrot, R.; Permingeat, F.; Ivanov, T. (1969): La raguinite $IFeS_2$, une nouvelle espèce minérale et le problème de l'allcharite: Persée - Portail des revues scientifiques en SHS. 92, 38–48 (in French).

Libowitzky, E.; Giester, G.; Tillmanns, E. (1995): The crystal structure of jankovićite, $Tl_5Sb_9(As,Sb)_4S_{22}$.European Journal of Mineralogy, 7, 479–488.

Lottermoser, B. G. (2010): Sulfidic Mine Wastes. In mine wastes. Springer, Berlin, Heidelberg. 43–117.

Majzlan, J.; Haase, P.; Plášil, J.; Dachs, E. (2019): Synthesis and stability of some members of the pharmacosiderite group, $AFe_4(OH)_4(AsO_4)_3{\cdot}nH_2O$ (A = K, Na, 0.5Ba, 0.5Sr). The Canadian Mineralogist, 57, 663–675.

Makreski, P., Jovanovski, G, Boev, B. (2014): Micro-Raman spectra of extremely rare and endemic Tl-sulfosalts from Allchar deposit. Journal of Raman Spectroscopy, 45, 610–617.

Manceau, A.; Simionovici, A.; Findling, N.; Glatzel, P.; Detlefs, B.; Wegorzewski, A. V.; Koschinsky, A. (2022): Crystal chemistry of thallium in marine ferromanganese deposits. ACS Earth and Space Chemistry, 6, 1269--1285.

McCarty, K. M.; Hanh, H. T.; Kyoung-Woong, K. (2011): Arsenic geochemistry and human health in South East Asia. Reviews on Environmental Health, 26, 71–78.

Mills, S. J.; Hager, S. L.; Leverett, P.; Williams, P. A.; Raudsepp, M. (2010a): The structure of H_3O^+-exchanged pharmacosiderite. Mineralogical Magazine, 74, 487–492.

Mills, S. J.; Kampf, A. R.; Williams, P. A.; Leverett, P.; Poirier, G.; Raudsepp, M.; Francis, C. A. (2010b): Hydroniumpharmacosiderite, a new member of the pharmacosiderite supergroup from Cornwall, UK: structure and description. Mineralogical Magazine, 74, 863–869.

Mills, S. J.; Rumsey, M. S.; Favreau, G.; Spratt, J.; Raudsepp, M; Dini M. (2011): Bariopharmacoalumite, a new mineral species from Cap Garonne, France and Mina Grande, Chile. Mineralogical Magazine, 75, 135–144.

Mills, S. J.; Meisser, N.; Rumsey, M. S.; Hay, D. G.; Spratt, J.; Ansermet, S.; Vonlanthen, P. (2014): Strontiopharmacosiderite, IMA 2013-101. CNMNC Newsletter 19. Mineralogical Magazine, 78, 165–170.

Mills, S. J.; Petrini, E.; Bellatreccia; F.; Schluter, J.; Kampf, A. R. et al. (2013): Caesiumpharmacosiderite, IMA 2013-096. CNMNC Newsletter 18. Mineralogical Magazine, 77, 3249-3258.

Moëlo, Y.; Biagioni, C. (2020): Contribution to the crystal chemistry of lead-antimony sulfosalts: systematic Pb-versus-Sb crossed substitution in the plagionite homologous series, $Pb_{2N-1}(Pb_{1-x}Sb_x)_2(Sb_{1-x}Pb_x)_2Sb_6S_{13+2N}$. European Journal of Mineralogy, 32, 623–635.

Multani, R. S.; Feldmann, T.; Demopoulos, G. P. (2016): Antimony in the metallurgical industry: A review of its chemistry and environmental stabilization options. Hydrometallurgy, 164, 141–153.

Nagl, P.; Mader, D. (2019): X-ray fluorescence (XRF) and instrumental neutron activation analysis (INAA) for the geochemical analysis of rocks, presented on in-house control samples. Mitteilungen der Österreichischen Mineralogischen Gesellschaft, 165, 67.

Nasdala, L.; Schmidt, C. (2020): Applications of Raman Spectroscopy in Mineralogy and Geochemistry: GeoScienceWorld (16). In Elements (2), 99–104.

Nordstrom, K. D. (2002): Public health. Worldwide occurrences of arsenic in ground water (296). In Science (New York, N.Y.) (5576), 2143–2145.

Palinkaš, S.; Hofstra, A. H.; Percival, T. J.; Šoštarkć, S. B.; Palinkaš, L.; Bermanec, V.; Pecskay, V.; Boev, B. (2018): Comparison of the Allchar Au-As-Sb-Tl Deposit, Republic of Macedonia, with Carlin-Type Gold Deposits. In Cline, J. S. (2018): Diversity of Carlin-style gold deposits. J. L. Muntean (Ed.). Society of Economic Geologists, Incorporated.

Pašava, J.; Pertlik, F.; Stumpfl, E. F.; Zemann, J. (1989): Bernardite, a new thallium arsenic sulphosalt from Allchar, Macedonia, with a determination of the crystal structure. Mineralogical Magazine, 53, 531–538.

Pavićević, M. K.; El Goresy, A. (1988): Crven Dol Tl deposit in Allchar. Mineralogical investigation, chemical composition of Tl minerals and genetic implications. Nuclear Instruments and Methods in Physics Research Section A: Accelerators, Spectrometers, Detectors and Associated Equipment, 271, 297–300.

Peacor, D. R.; Dunn, P. J. (1985): Sodium-pharmacosiderite, a new analog of pharmacosiderite from Australia and new occurrences of barium-pharmacosiderite. Mineralogical Record, 16, 121–124.

Percival, T. J.; Radtke, A. S. (1994): Sedimentary-rock-hosted disseminated gold mineralization in the Alsar District, Macedonia. The Canadian Mineralogist, 32, 649–665.

Peter, J. A. L.; Viraraghavan, T. (2005): Thallium: a review of public health and environmental concerns. Environment International, 31, 493–501.

Raber, T.; Roth, P. (2018): The Lengenbach quarry in Switzerland: classic locality for rare thallium sulfosalts. Minerals, 8, 409–416.

Rieck, B. (1993): Famous Mineral Localities: Allchar, Macedonia. Mineralogical Record, 24, 437–449.

Roper, A.J.; Williams, P.A.; Filella, M. (2012): Secondary antimony minerals: phases that control the dispersion of antimony in the supergene zone. Geochemistry, 72, 9–14.

Rumsey, M.S.; Mills, S.J.; Spratt, J. (2010): Natropharmacoalumite, $NaAl_4[(OH)_4(AsO_4)_3]\cdot 4H_2O$, a new mineral of the pharmacosiderite supergroup and the renaming of aluminopharmacosiderite to pharmacoalumite. Mineralogical Magazine, 74, 929–936.

Rumsey, M. S.; Mills, S. J.; Spratt, J.; Hay, D. G.; Farber, G. (2014): Thalliumpharmacosiderite. Mineralogical Magazine, 78, 549–558.

Schofield, P. F.; Knight, K. S.; Stretton, I. C. (1996): Thermal expansion of gypsum investigated by neutron powder diffraction. American Mineralogist, 81, 847–851.

Skoog, D. A.; Leary, J. J. (2013): Instrumentelle Analytik: Grundlagen-Geräte-Anwendungen. Springer-Verlag, 1--901.

Smichowski, P. (2008): Antimony in the environment as a global pollutant: a review on analytical methodologies for its determination in atmospheric aerosols. Talanta, 75, 2–14.

Spieß, L.; Teichert, G.; Schwarzer, R.; Behnken, H.; Genzel, C. (2019): Moderne Röntgenbeugung. Röntgendiffraktometrie für Materialwissenschaftler, Physiker und Chemiker. Springer-Verlag, 1--652.

Vignola, P.; Rotiroti, N.; Hatert, F.; Dal Bo, F.; Gentile, P.; Albertini, C.; Merlini, M.; Risplendente, A.; Pavese, A (2018): Plumbopharmacosiderite, $Pb_{0.5}\ Fe^{3+}_4\ (AsO_4)_3(OH)_4\cdot 5H_2O$, a new mineral species from the Monte Falò Pb-Zn mine near the village of Coiromonte in the Armeno Municipality, Novara Province, Italy. The Canadian Mineralogist, 56, 143–150.

Voegelin, A.; Pfenninger, N.; Petrikis, J.; Majzlan, J.; Plötze, M.; Senn, A. C.; Mangold, S.; Steininger, R.; Göttlicher, J. (2015): Thallium speciation and extractability in a thallium- and arsenic-rich soil developed from mineralized carbonate rock. Environmental Science and Technology, 49, 5390–5398.

Volkov, A. V.; Serafimovski, T.; Kochneva, N. T.; Tomson, I. N.; Tasev, G. (2006): The Alshar epithermal Au-As-Sb-Tl deposit, southern Macedonia. Geology of Ore Deposits, 48, 175–192.

Wick, S.; Baeyens, B.; Fernandes, M.M.; Voegelin, A. (2018): Thallium adsorption onto illite. Environnemental Science and Technology, 52, 571–580.

Wick, S.; Peña, J.; Voegelin, A. (2019): Thallium sorption onto manganese oxides. Environnemental Science and Technology, 53, 13168–13178.

Wick, S.; Baeyens, B.; Fernandes, M. M.; Göttlicher, J.; Fischer, M.; Pfenninger, N.; Plötze, M.; Voegelin, A. (2020): Thallium sorption and speciation in soils: Role of micaceous clay minerals and manganese oxides. Geochimica et Cosmochimica Acta, 288, 83-100.

Wilson, J.; Sen Gupta, P.; Robinson, P.; Criddle, A. (1993): Fangite, Tl_3AsS_4, a new thallium arsenic sulfosalt from the Mercur Au deposit, Utah, and revised optical data for gillulyite. American Mineralogist, 78, 1096–1103.

Xiao, T.; Guha, J.; Boyle, D.; Liu, C.; Zheng, B.; Wilson, G. C.; Rouleau, A.; Chen, J. (2004): Naturally occurring thallium: a hidden geoenvironmental health hazard. Environment International, 30, 501–507.

Xiong, Y. (2009): The aqueous geochemistry of thallium: speciation and solubility of thallium in low temperature systems. Environmental Chemistry, 6, 441–451.

Yakovenchuk, V.N.; Nikolaev, A.P.; Selivanova, E.A.; Pakhomovsky, Y.A.; Korchak, J.A.; Spiridonova, D.V.; Zalkind, O.A.; Krivovichev, S.V. (2009): Ivanyukite-Na-T, ivanyukite-Na-C, ivanyukite-K, and ivanyukite-Cu: New microporous titanosilicates from the Khibiny massif (Kola Peninsula, Russia) and crystal structure of ivanyukite-Na-T. American Mineralogist, 94, 1450–1458.

Zhao, F.; Gu, S. (2021): Secondary sulfate minerals from thallium mineralized areas: Their formation and environmental significance. Minerals, 11, 855–870.

Zhuang, W.; Liu, M.; Song, J.; Ying, S. C. (2021): Retention of thallium by natural minerals: a review: Science of the Total Environment, 777, 146074–146082.

Appendices

Appendix 1: List of all minerals found in Allchar

Mineral	Type	Formula	Reference
Ankerite	Primary	$Ca(Fe^{2+},Mg)(CO_3)_2$	Balić Žunić et al., 1993
Arseniosiderite [2]	Secondary	$Ca_2Fe^{3+}_3(AsO_4)_3O_2 \cdot 3H_2O$	Đorđević et al., 2021; this work
Avicennite [1]	Primary	Tl_2O_3	This work
Bernardite	Primary	$TlAs_5S_8$	Pašava et al., 1989
Biotite [2]	Secondary	$K(Mg,Fe)_3AlSi_3O_{10}(OH)_2$	Boev and Boev, 2015; this work
Calcite [1 2]	Gangue	$CaCO_3$	Rieck, 1993; this work
Christite	Primary	$TlHgAsS_3$	Đorđević et al., 2020
Cinnabar [2]	Primary	HgS	Boev et al., 2001; this work

Claudetite	Secondary	As_2O_3	Boev et al., 2001
Dolomite [1 2]	Primary	$CaMg(CO_3)_2$	Balić Žunić et al., 1993; this work
Dorallcharite [1 2]	Secondary	$TlFe_3^{+3}(SO_4)_2(OH)_6$	Balić-Žunić et al., 1994; this work
Fangite [2]	Primary	Tl_3AsS_4	El Goresy and Pavicevic, 1988; Frantz et al., 1994; this work
Fibroferrite	Secondary	$Fe^{3+}(SO_4)(OH) \cdot 5H_2O$	Boev and Boev, 2015
Goethite [1]	Secondary	α-$Fe^{3+}O(OH)$	Rieck, 1993; this work
Gold	Primary	Au	Rieck, 1993
Gypsum [1]	Gangue	$CaSO_4 \cdot 2H_2O$	Boev et al., 2001; this work
Hörnesite	Secondary	$Mg_3(AsO_4)_2 \cdot 8H_2O$	Rieck, 1993
Hydroniumjarosite [2]	Secondary	$(H_3O)Fe^{3+}{}_3(SO_4)_2(OH)_6$	Đorđević et al., 2021; this work
Hydroniumpharmacosiderite [2]	Secondary	$(H_3O)Fe_4(AsO_4)_3(OH)_4 \cdot 4H_2O$	Đorđević et al., 2021; this work

Jankovićite	Primary	$Tl_5Sb_9(As,Sb)_4S_{22}$	Cvetković et al., 1995; Libowitzky et al., 1995
Jarosite [2]	Secondary	$KFe^{3+}{}_3(SO_4)_2(OH)_6$	Đorđević et al., 2021; this work
Lorándite [1 2]	Primary	$TlAsS_2$	Krenner, 1897; this work
Marcasite [1]	Primary	FeS_2	Rieck, 1993, this work
Muscovite [1 2]	Secondary	$KAl_2(AlSi_3O_{10})(OH)_2$	Percival and Radke, 1994
Natropharmacosiderite	Secondary	$Na_2Fe^{3+}{}_4(AsO_4)_3(OH)_5 \cdot 7H_2O$	Majzlan et al., 2019
Orpiment [2]	Primary	As_2S_3	Percival and Radke, 1994; this work
Parapierrotite	Primary	$TlSb_5S_8$	John et al., 1995
Pararealgar	Primary	As_4S_4	Rieck, 1993
Pharmacosiderite[1]	Secondary	$KFe^{3+}{}_4(AsO_4)_3(OH)_4 \cdot 6\text{-}7H_2O$	Percival and Radke, 1994; this work
Thalliumpharmaco-siderite [2]	Secondary	$TlFe^{3+}{}_4(AsO_4)_3(OH)_4 \cdot 4H_2O$	Rumsey et al., 2014; this work

Pictopaulite	Primary	$TlFe_2S_3$	Balić-Žunić et al., 2008
Picropharmacolite	Secondary	$Ca_4Mg(AsO_4)_2(HAsO_4)_2 \cdot 11H_2O$	Rieck, 1993
Plagionite	Primary	$Pb_5Sb_8S_{17}$	Boev and Boev 2015
Pyrite [1 2]	Primary	FeS_2	Rieck, 1993; this work
Pyrrhotite	Primary	$Fe_{1-x}S$	Đorđević et al., 2021
Quartz [1]	Gangue	SiO_2	Rieck, 1993; this work
Raguinite	Primary	$TlFeS_2$	Laurent et al., 1969
Realgar [1 2]	Primary	As_4S_4	Rieck, 1993; this work
Rebulite	Primary	$Tl_5Sb_5As_8S_{22}$	Balić-Žunić et al., 2015
Sanidine [1]	Primary	$K(AlSi_3O_8)$	Boev and Boev, 2015; this work
Scorodite [1]	Secondary	$Fe^{3+}AsO_4 \cdot 2H_2O$	Parcival and Radke, 1994; this work
Siderite [2]	Primary	$FeCO_3$	Balić Žunić et al., 1993; this work

Silver	Primary	Ag	Boev and Boev, 2015
Simonite	Primary	$TlHgAs_3S_6$	Engel et al., 1982
Starkeyite	Secondary	$MgSO_4 \cdot 4H_2O$	Rieck, 1993
Stibnite	Primary	Sb_2S_3	Rieck, 1993
Talmessite [2]	Secondary	$Ca_2Mg(AsO_4)_2 \cdot 2H_2O$	Đorđević et al. 2021; this work
Vrbaite	Primary	$Hg_3Tl_4As_8Sb_2S_{20y}$	Boev et al., 2001
Weissbergite	Primary	$TlSbS_2$	Rieck, 1993
new! Tl-M^{2+}-arsenates[1]		(M=Mg,Mn,Fe,Ca) Tl:*M*:As ~1,5:1:1,5	This work
new! Tl-M^{2+}-arsenates[1]		(M=Mg,Mn,Fe,Ca) Tl:*M*:As ~ 2:1:1	This work
new! Tl-M^{2+}-arsenates[1]		With Si and Al	This work

[1)] PXRD [2)] SEM-EDX

Appendix 2: SEM EDX Data Sample 4 – Thallium Secondary Minerals

Element	O [at. %]	Na [at. %]	Mg [at. %]	Al [at. %]	Si [at. %]	P [at. %]	S [at. %]	K [at. %]	Ca [at. %]	Mn [at. %]	Fe [at. %]	As [at. %]	Ba [at. %]	Tl [at. %]
Tl-M^{2+}As - (CD-18-4)	51		4.0	1.1					1.9	3.8	3.5	11.8		23.0
Tl-M^{2+}As - (CD-18-4)	50	0.3	4.0	0.5					2.1	5.8	4.0	11.9		21.5
Tl-M^{2+}As - (CD-18-4)	54	0.4	3.4	2.1					1.8	4.6	3.5	10.7		19.9
Tl-M^{2+}As - (CD-18-4)	54			3.7	6.8			0.7	2.4	1.6	1.7	9.0		20.1
Tl-M^{2+}As - (CD-18-4)	56		1.7	5.5	6.7			0.4	2.3	1.4	1.8	7.4		17.1
Tl-M^{2+}As - (CD-18-4)	51		2.3	1.3	2.7				2.9	1.7	2.4	10.0		26.0
Tl-M^{2+}As - (CD-18-4)	54		2.4	3.8	4.4			0.7	2.8	0.8	3.2	7.9		19.7
Tl-M^{2+}As - (CD-18-4)	53	0.6	2.1	5.4	0.7				2.6	1.1	3.6	8.4		22.1
TlAsO? - (CD-18-4)	59								3.0	1.4	2.0	10.2		24.7
Tl-M^{2+}As - (CD-18-4)	51		2.8						2.2	0.5	1.0	10.5		31.8
Tl-M^{2+}As - (CD-18-4)	53		2.1						2.7	0.8	1.7	10.2		30.0
Tl-M^{2+}As - (CD-18-4)	54		2.5						2.6	0.8	2.3	10.1		27.7
Tl-M^{2+}As - (CD-18-4)	54		2.7						3.0	0.4	2.1	10.6		27.5
Tl-M^{2+}As - (CD-18-4)	54		2.8						2.4	0.3	1.1	10.1		29.1
Tl-Met^{2+}AsO - (CD-18-4)	52		2.1	0.6					3.2	2.3	1.8	10.8		27.6
Sco+Tl? - (CD-18-4)	69			1.0					0.3		12.4	15.5		1.7
Sco+Tl? - (CD-18-4)	69	0.2	0.3	1.5		0.1			0.2		11.9	15.5		1.2
MnOxide+Ca,Tl - (CD-18-4)	60		0.5	0.3			0.8		3.9	28.7	0.8	1.0		3.8
MnOxide+Ca,Tl - (CD-18-4)	61		0.5		0.2		0.8		3.5	28.8	1.0	0.7	0.1	3.6
MnOxide+Ca,Tl - (CD-18-4)	64		0.6	0.5	0.7				3.5	25.6	1.1	0.7		3.1
Tl-MnAsrenate - (CD-18-4)	58		1.6	1.8	3.6	0.6			4.8	9.5	2.4	10.0		7.9
Tl-MnArsenate - (CD-18-4)	64		1.4	0.9	2.7	0.4			4.6	9.8	1.9	9.6		5.0

Appendix 3: SEM -EDX Data Sample 6A– Secondary arsenic minerals

Spectrum	O [wt.%]	Mg [wt.%]	Al [wt.%]	Si [wt.%]	P [wt.%]	S [wt.%]	K [wt.%]	Ca [wt.%]	Mn [wt.%]	Fe [wt.%]	As [wt.%]	Tl [wt.%]
TlMnAsrenate - CD-18-6A	58	1.6	1.8	3.6	0.6			4.8	9.5	2.4	10.0	7.9
Dolomit+TraceMnFe - CD-18-6A	73	11.6						14.7	0.4	0.4		
CaMnArsenate - CD-18-6A	68		0.4	0.6		0.4		8.8	10.3	0.5	11.4	
CaMnArsenate - CD-18-6A	66		0.6	1.3		0.4	0.1	8.8	9.3	1.3	11.8	
CaMnArsenate - CD-18-6A	67		0.3	0.6		0.3		9.0	11.1		12.1	
CaMnArsenate - CD-18-6A	66		1.4	1.8		0.2	0.2	8.8	9.7	0.7	11.3	0.1
CaMnArsenate - CD-18-6A	69		0.8	0.7				8.6	10.1	0.5	10.5	0.1

Appendix 4: SEM -EDX Data Sample 4–Secondary arsenic minerals

Element	O [at. %]	Na [at. %]	Mg [at. %]	Al [at. %]	Si [at. %]	P [at. %]	K [at. %]	Ca [at. %]	Mn [at. %]	Fe [at. %]	As [at. %]	Tl [at. %]
Tl-M^{2+} - Arsenate (CD-4A)	51		4.0	1.1				1.9	3.8	3.5	11.8	23.0
Tl-M^{2+} - Arsenate (CD-4A)	50	0.3	4.0	0.5				2.1	5.8	4.0	11.9	21.5
Tl-M^{2+} - Arsenate (CD-4A)	54	0.4	3.4	2.1				1.8	4.6	3.5	10.7	19.9
Tl-M^{2+} - Arsenate (CD-4A)	54			3.7	6.8		0.7	2.4	1.6	1.7	9.0	20.1
Tl-M^{2+} - Arsenate (CD-4A)	56		1.7	5.5	6.7		0.4	2.3	1.4	1.8	7.4	17.1
Tl-M^{2+} - Arsenate (CD-4A)	51		2.3	1.3	2.7			2.9	1.7	2.4	10.0	26.0
Tl-M^{2+} - Arsenate (CD-4A)	54		2.4	3.8	4.4		0.7	2.8	0.8	3.2	7.9	19.7
Tl-M^{2+} - Arsenate (CD-4A)	53	0.6	2.1	5.4	0.7			2.6	1.1	3.6	8.4	22.1
Tl-M^{2+} - Arsenate (CD-4A)	59							3.0	1.4	2.0	10.2	24.7
Tl-M^{2+} - Arsenate (CD-4A)	51		2.8					2.2	0.5	1.0	10.5	31.8
Tl-M^{2+} - Arsenate (CD-4A)	53		2.1					2.7	0.8	1.7	10.2	30.0
Tl-M^{2+} - Arsenate (CD-4A)	54		2.5					2.6	0.8	2.3	10.1	27.7
Tl-M^{2+} - Arsenate (CD-4A)	54		2.7					3.0	0.4	2.1	10.6	27.5
Tl-M^{2+} - Arsenate (CD-4A)	54		2.8					2.4	0.3	1.1	10.1	29.1
Tl-M^{2+} - Arsenate (CD-4A)	52		2.1	0.6				3.2	2.3	1.8	10.8	27.6
Tl-M^{2+} - Arsenate (CD-4A)	58		1.6	1.8	3.6	0.6		4.8	9.5	2.4	10.0	7.9
Tl-M^{2+} - Arsenate (CD-4A)	64		1.4	0.9	2.7	0.4		4.6	9.8	1.9	9.6	5.0

Appendix 5: Chemical composition (wt.-%) of major elements of the samples, measured by XRF

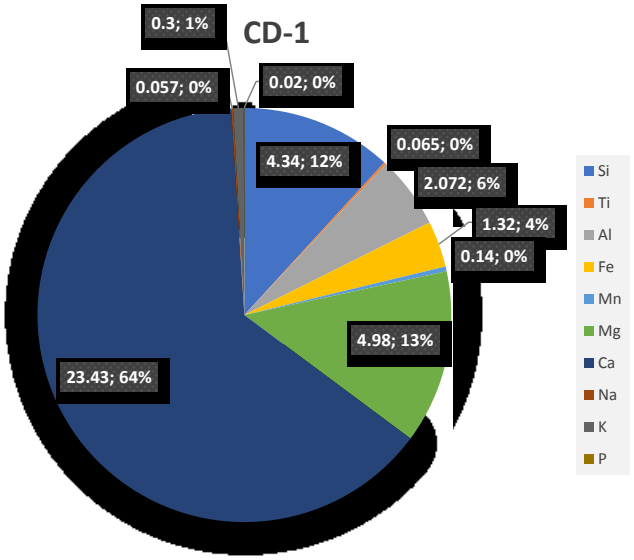

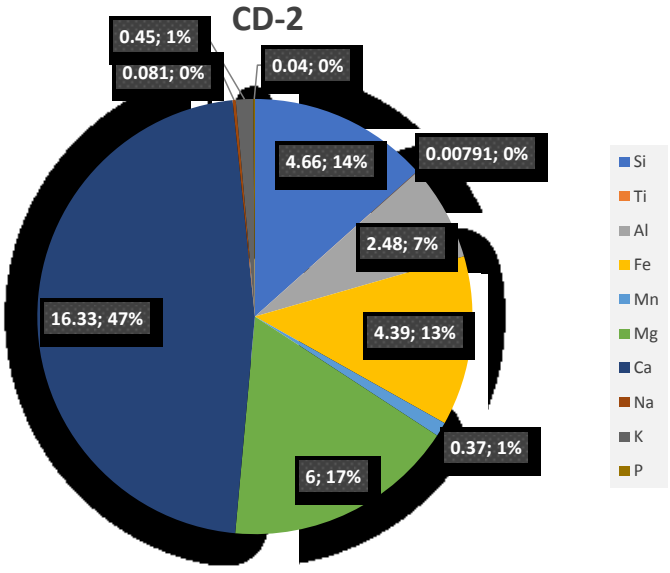

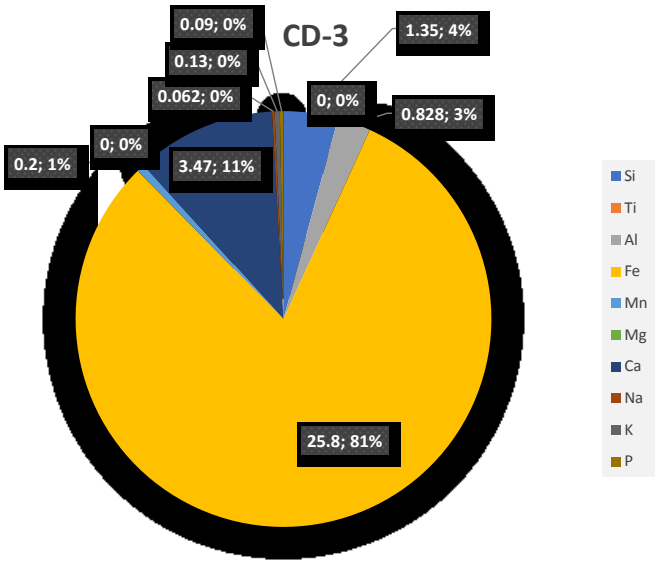
CD-3
0.09; 0%
1.35; 4%
0.13; 0%
0.062; 0%
0; 0%
0.828; 3%
0; 0%
0.2; 1%
3.47; 11%
25.8; 81%
Si
Ti
Al
Fe
Mn
Mg
Ca
Na
K
P

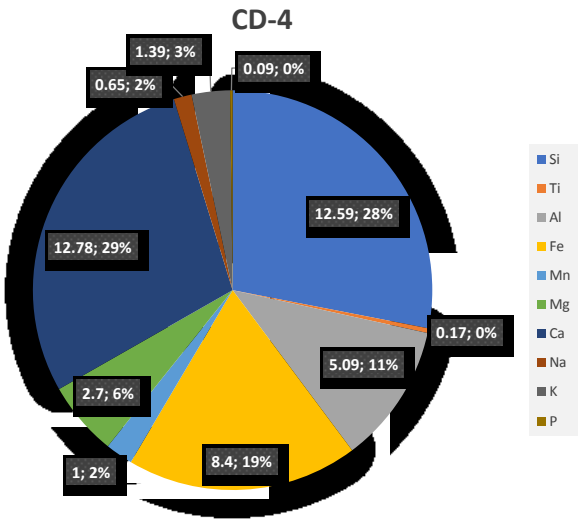
CD-4
1.39; 3%
0.09; 0%
0.65; 2%
12.59; 28%
12.78; 29%
0.17; 0%
5.09; 11%
2.7; 6%
8.4; 19%
1; 2%
Si
Ti
Al
Fe
Mn
Mg
Ca
Na
K
P

Appendix 6: Trace elements (in ppm) measured with XRF

Element	CD-18-1 [ppm]	CD-18-2 [ppm]	CD-18-3 [ppm]	CD-18-4 [ppm]
As	16,855.10	30,690.30	165,830.70	21,405.90
Ba	79.3	83.4	234.5	1205.3
Bi	<1	<1	<1	<1
Cd	3.3	3.1	5.2	5.3
Ce	116.7	174.5	364.0	165.4
Co	11.1	54.1	7.2	36.8
Cr	31.6	50.4	32.0	36.9
Cu	12.7	17.0	27.1	24.5
Ga	0.5	<1	<1	6.1
Hf	15.7	15.8	210.1	11.9
La	12.0	19.9	4.8	49.7
Mo	2.4	4.3	7.6	7.3
Nb	1.1	1.8	0.5	5.7
Nd	18.5	21.6	38.7	39.4
Ni	36.4	56.2	20.9	69.6
Pb	5.1	8.7	45.6	34.4
Rb	22.1	32.0	<1	89.9
Sb	110.8	10.2	10.1	20.0
Sc	<1	<1	1.3	<1
Sm	2.8	2.0	0.3	<1
Sn	3.1	4.1	7.0	7.1
Sr	42.3	51.7	26.1	205.6
Ta	<1	<1	<1	<1
Th	1.5	2.2	<1	16.2
Tl	979.5	969.0	10571.2	755.2
U	<1	1.6	<1	7.3
V	32.0	62.3	150.9	88.7
W	9.2	11.7	<1	7.2
Y	5.1	9.5	7.2	19.0
Yb	0.5	1.3	1.3	1.7
Zn	29.8	95.3	371.1	152.2
Zr	17.2	17.9	19.4	102.6

Appendix 7: Powder X-ray diffraction patterns of the samples CD-1, CD-2, CD-3, CD-4 and CD-18-3-HS, CD-18-3A-HS and CD-18-3A2-HS

Note: Pictures shown as listed in the heading

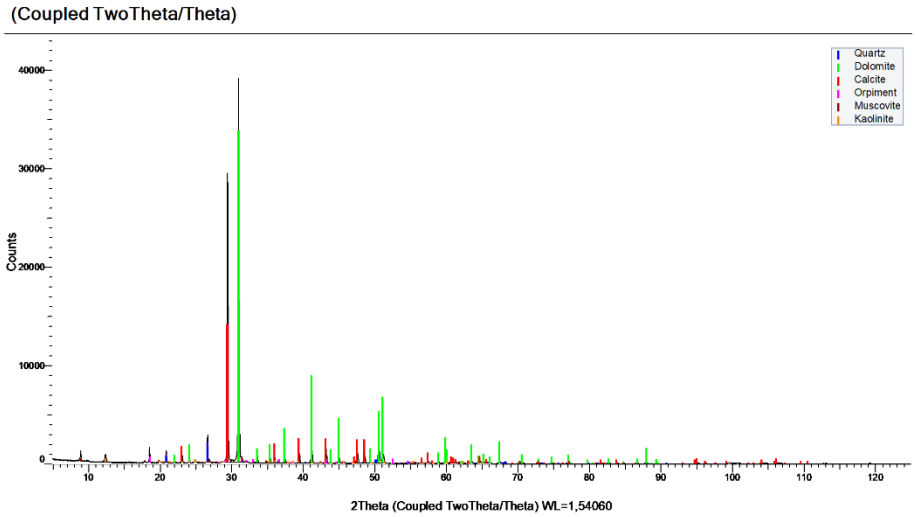

Sample CD-1

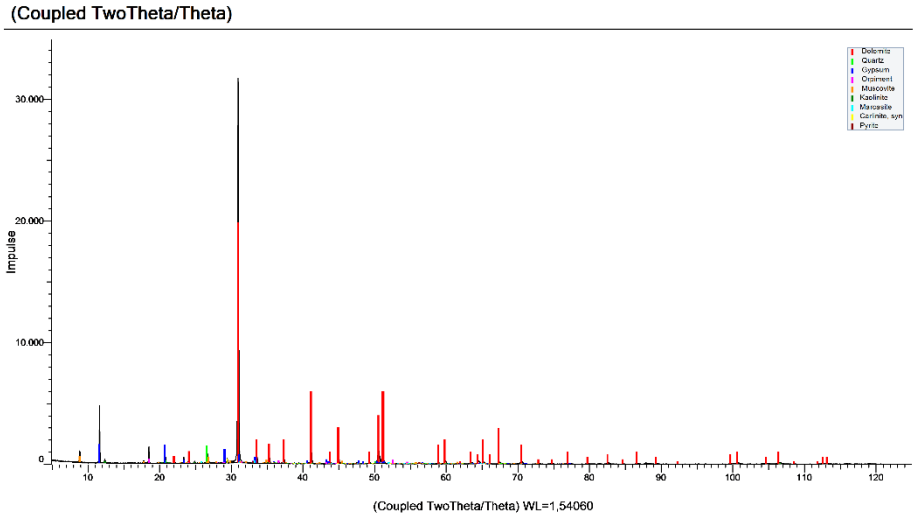

Sample CD-2

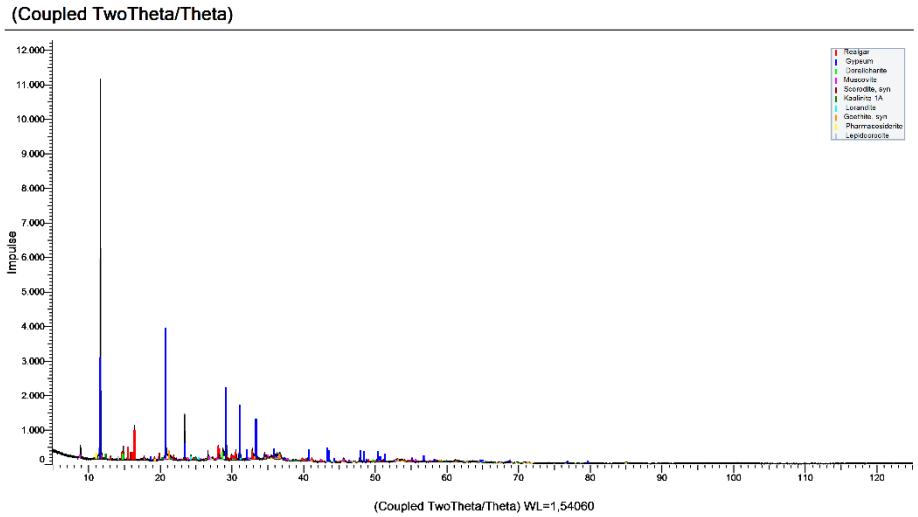

Sample CD-3

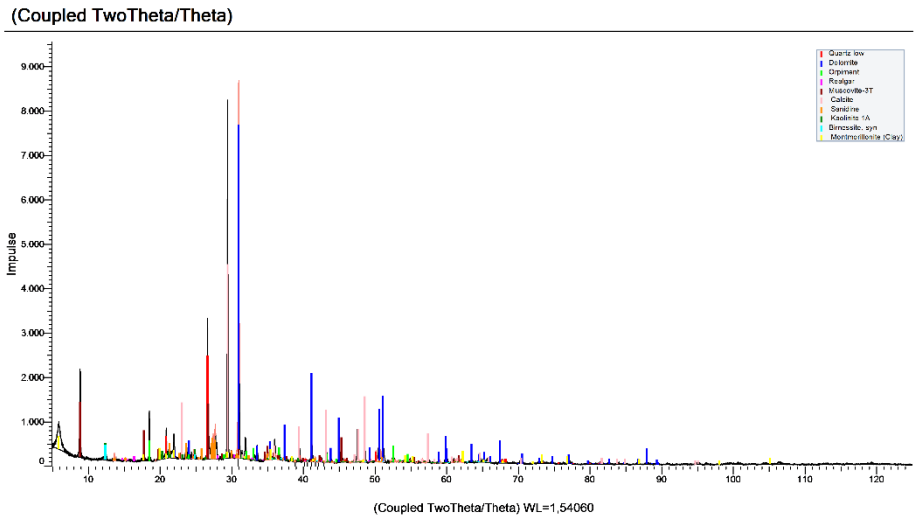

Sample CD-4

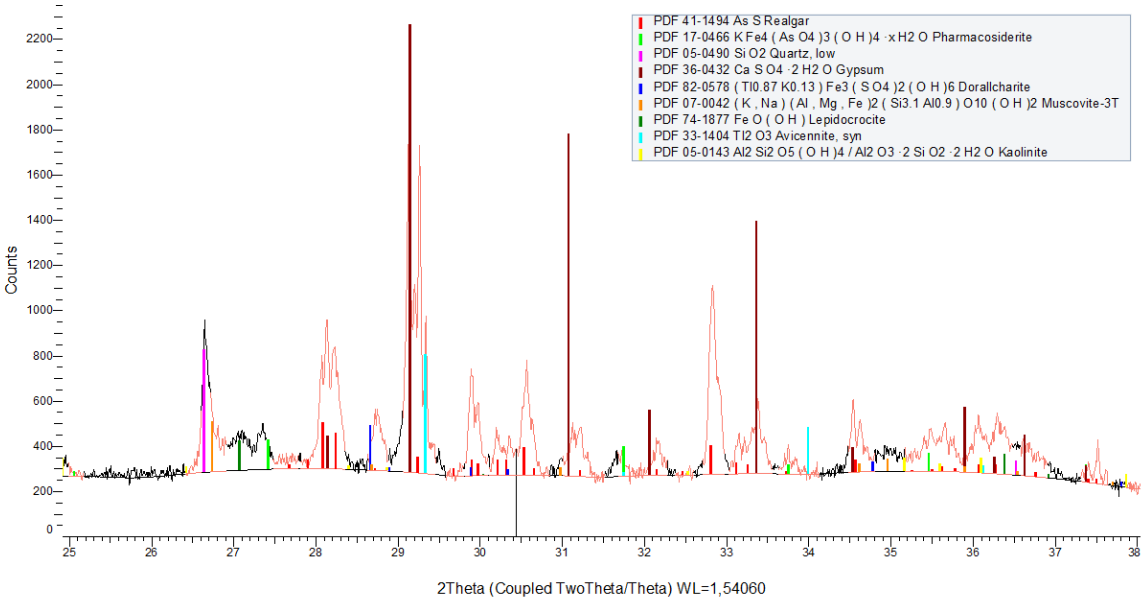

Sample CD-3-HS

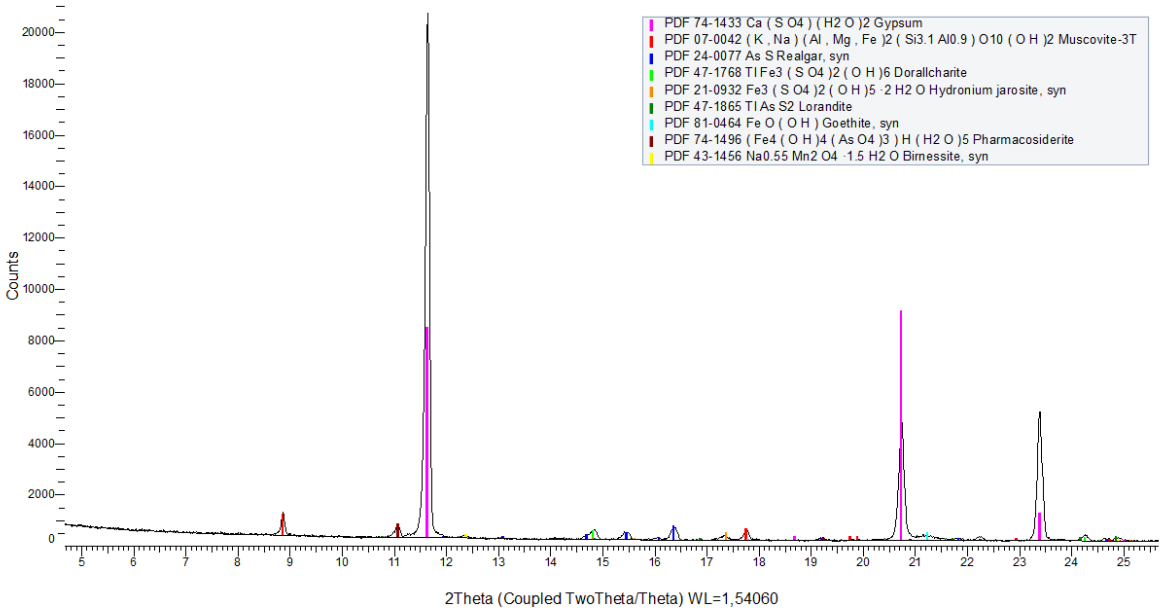

Sample CD-3A-HS

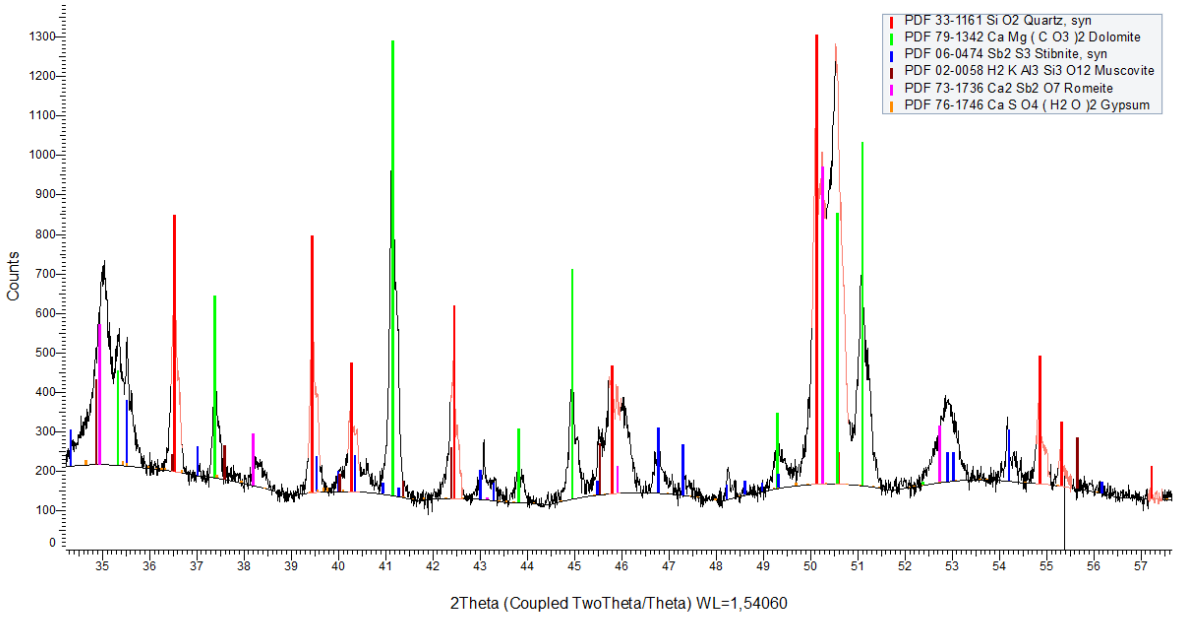

Sample CD-3A2-HS

Appendix 8: Picture of the powder pellets of the samples for XRF

Note: CD-18-1 → CD-1; CD-18-2 → CD-2; CD-18-3 →CD-3; CD-18-4 → CD-4

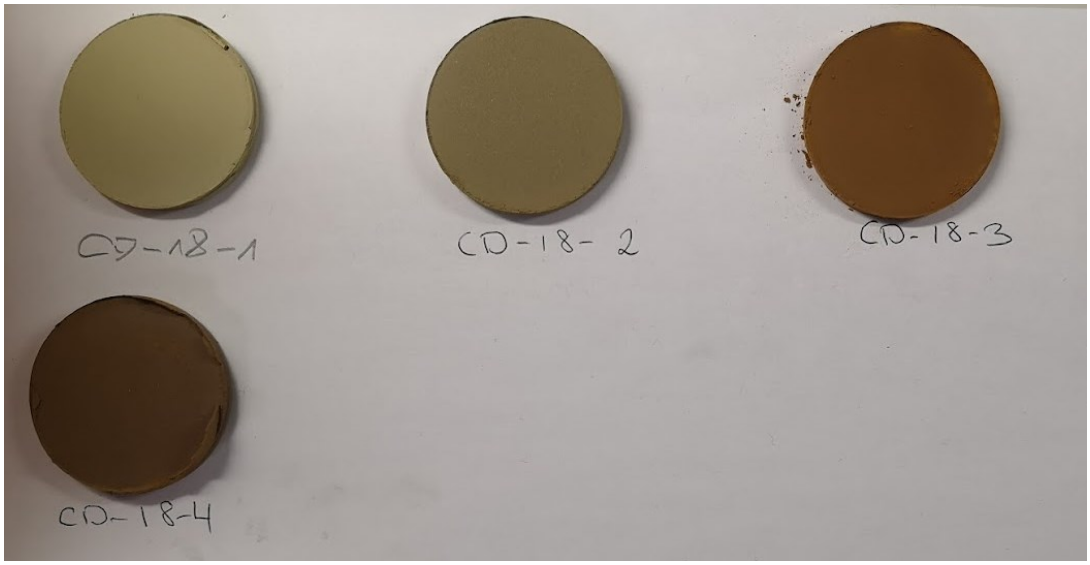

Appendix 9: Picture of polished samples for SEM-EDX and Raman

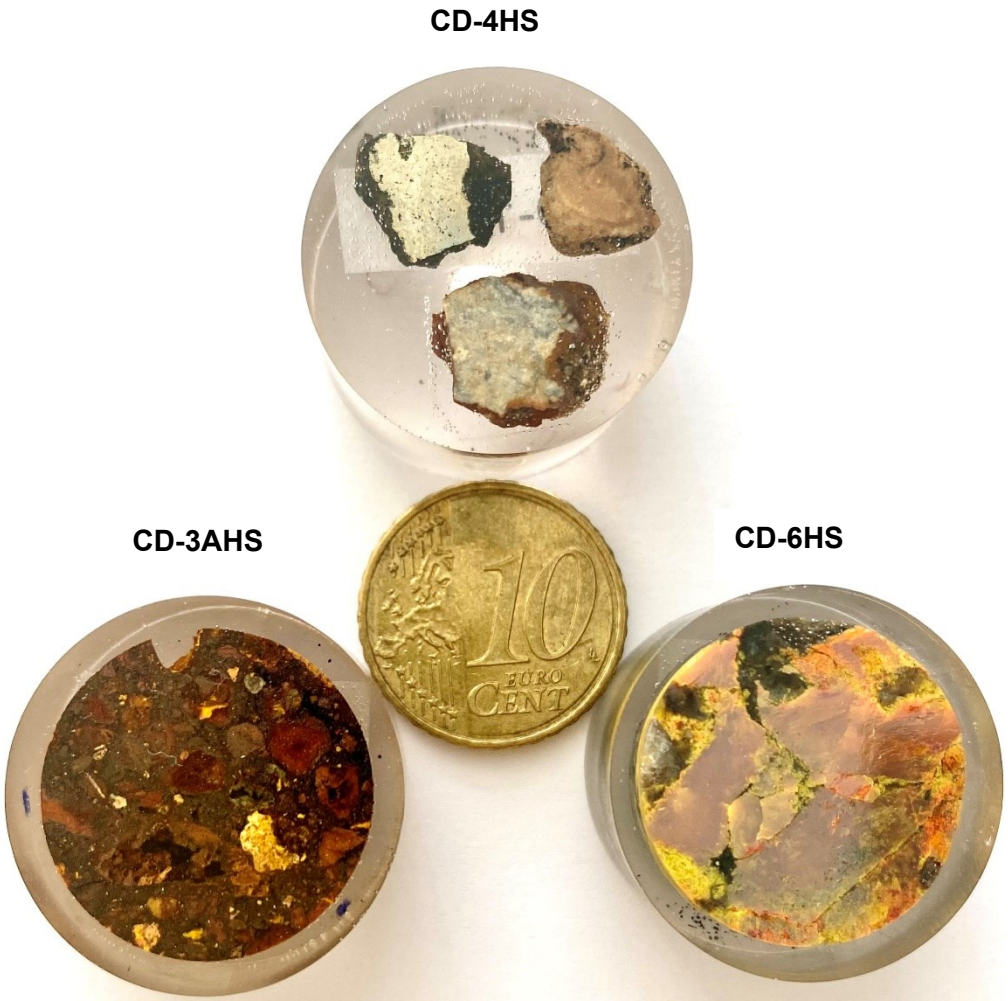

Appendix 10:

a) Bruker 08 diffractometer

b) Sample holder